

**When three is a crowd: Chaos from clusters of Kuramoto oscillators with inertia**Barrett N. Brister,<sup>1</sup> Vladimir N. Belykh,<sup>2,3</sup> and Igor V. Belykh <sup>1,3</sup><sup>1</sup>*Department of Mathematics and Statistics and Neuroscience Institute, Georgia State University,  
P.O. Box 4110, Atlanta, Georgia 30302-410, USA*<sup>2</sup>*Department of Mathematics, Volga State University of Water Transport, 5A Nesterov street, Nizhny Novgorod 603950, Russia*<sup>3</sup>*Department of Control Theory, Lobachevsky State University of Nizhny Novgorod, 23 Gagarin Avenue, Nizhny Novgorod 603950, Russia*

(Received 5 April 2020; accepted 1 June 2020; published 18 June 2020)

Modeling cooperative dynamics using networks of phase oscillators is common practice for a wide spectrum of biological and technological networks, ranging from neuronal populations to power grids. In this paper we study the emergence of stable clusters of synchrony with complex intercluster dynamics in a three-population network of identical Kuramoto oscillators with inertia. The populations have different sizes and can split into clusters where the oscillators synchronize within a cluster, but notably, there is a phase shift between the dynamics of the clusters. We extend our previous results on the bistability of synchronized clusters in a two-population network [I. V. Belykh *et al.*, *Chaos* **26**, 094822 (2016)] and demonstrate that the addition of a third population can induce chaotic intercluster dynamics. This effect can be captured by the old adage “two is company, three is a crowd,” which suggests that the delicate dynamics of a romantic relationship may be destabilized by the addition of a third party, leading to chaos. Through rigorous analysis and numerics, we demonstrate that the intercluster phase shifts can stably coexist and exhibit different forms of chaotic behavior, including oscillatory, rotatory, and mixed-mode oscillations. We also discuss the implications of our stability results for predicting the emergence of chimeras and solitary states.

DOI: [10.1103/PhysRevE.101.062206](https://doi.org/10.1103/PhysRevE.101.062206)**I. INTRODUCTION**

Patterns of synchronized activities are observed in many natural and technological networks [1–3]. In biological systems, examples include synchronized cortical rhythms in the central nervous systems of mammals which are crucial for sensory perception, memory, and locomotion [4–6]; pathological neuronal synchronization, which causes epileptic seizures and Parkinson’s tremors [7,8]; birds flying in formation and maneuvering as one cohesive unit [9]; and synchronized gaits of walkers on a wobbly footbridge [10–13]. In technological systems, synchronization is required for an array of lasers to reach high intensity levels [14–16] and for power generators for the operation of electrical power grids [17].

The strongest form of synchronized activities is complete synchronization of identical or nearly identical oscillators whose emergence and stability are controlled by the underlying network structure [18–21]. Cluster synchronization emerges when the network splits into clusters of coherent oscillators but the dynamics between the clusters remains asynchronous [22–33]. The existence of clusters in networks of identical oscillators is governed by network symmetries, and possible cluster partitions can be identified by combinatorial methods [31–33]. The stability of cluster synchronization [22–25,30,33] and its persistence against individual oscillators’ parameter mismatch [26] have been studied for several general classes of oscillator networks. However, the emergence and hysteretic transitions between clusters in multistable oscillator networks have yet to be fully understood. The celebrated Kuramoto model of first-order phase oscillators [34,35] is such an example of a network capable of exhibiting

various transitions from complete incoherence to cluster and complete synchronization [36–43]. These transitions are often accompanied by the emergence of spatiotemporal structures such as chimeras in which some oscillators synchronize within a cluster whereas the others remain in incoherent states [44–47]. While completely rigorous analysis of the stability of chimera states in Kuramoto networks is often elusive and most studies rely on numerical simulations, there are a select few that put this analysis for large [48–50] and small [51,52] networks on a more rigorous footing.

The original Kuramoto model of one-dimensional (1D) oscillators was extended to a model of two-dimensional (2D) phase oscillators with inertia [53]. This modification made the 2D oscillators capable of adjusting their natural frequencies and allowed the Kuramoto second-order oscillator network to become a more adequate model of real-world networks, including neural, mechanical, and power grid systems [54]. As a result, networks of Kuramoto oscillators with inertia can exhibit a rich array of dynamics, including complex synchronization transitions [55–58], hysteresis [59] and bistability of synchronous clusters [60], intermittent chaotic chimeras [61], reentrant synchronous regimes [62], and solitary states [63,64]. In particular, it was numerically demonstrated that weak chimera states can appear in small networks composed of only three Kuramoto oscillators with inertia [64]. These so-called weak chimera states are characterized by the formation of a synchronized two-oscillator cluster and one incoherent oscillator which rotates at a different frequency and can exhibit periodic or chaotic dynamics [64]. The smallest chimera states in the three-node network can also be viewed as a proxy of a two-cluster pattern in a three-group network of

identical Kuramoto oscillators with inertia. In this setting, the oscillators can synchronize within each group, and two groups in turn can synchronize between each other while leaving the dynamics of the third group incoherent. The emergence of these and more complex clusters of synchrony in multipopulation Kuramoto networks with inertia calls for an analytical study to isolate the principal bifurcations and stability mechanisms underpinning the coexistence of stable clusters with complex, possibly chaotic dynamics. This paper seeks to establish such an analytical insight.

In a recent paper [60], we derived analytical conditions for the emergence and coexistence of stable synchronized clusters in a two-population network of identical Kuramoto oscillators with inertia. These populations have different sizes such that complete synchronization of all oscillators is impossible. Instead, the oscillators can synchronize within each population cluster while there is a phase shift between the dynamics of the two clusters. Due to the presence of the inertia which makes the oscillator dynamics two-dimensional, this phase shift can oscillate, inducing a breathing cluster pattern which can stably coexist with a cluster pattern with a constant phase shift. In this paper, we aim at cluster dynamics of a three-population Kuramoto network with inertia obtained by adding a third population to the above two-population network setting from [60]. The resultant network is a three-population network of oscillators capable of synchronizing within each population, thereby potentially forming three synchronized clusters.

We primarily focus on the intercluster phase dynamics, which can exhibit various types of complex behavior and multistability. Through rigorous analysis and numerics, we demonstrate that the addition of the third population can induce multistable chaotic dynamics, including those in which the phase shift between the first and second populations oscillates chaotically with small amplitudes, whereas the phase shift between the second and third populations makes large-amplitude chaotic excursions. This effect may remind the reader of the familiar expression about romantic relationships “two is company, three is a crowd.” This conventional wisdom suggests how events may unfold when such a relationship becomes destabilized by the addition of a third party.

Our three-population network can be considered a phenomenological model for describing cluster formation in real-world oscillatory networks. Suitable real-world network dynamics that can be captured by our model include (i) a multicommodity neural structure of the nematode *Caenorhabditis elegans* in which neurons within each community form clusters of synchronized electrical activity that control locomotory rhythmogenesis [65,66] and (ii) animal grouping when schooling fish align their swimming directions to split into cooperative clusters of synchronized movements to improve foraging success [67].

The layout of this paper is as follows. First, in Sec. II, we present the oscillator network model and state the problem under consideration. In Sec. III, we study limit sets and bifurcations in a four-dimensional (4D) system of two coupled pendulum equations which determines the existence of possible intercluster dynamics in the three-population network. We develop an auxiliary system method to derive bounds on partitions of parameters with permissible dynamics which include combinations of coexisting constant, periodic, and

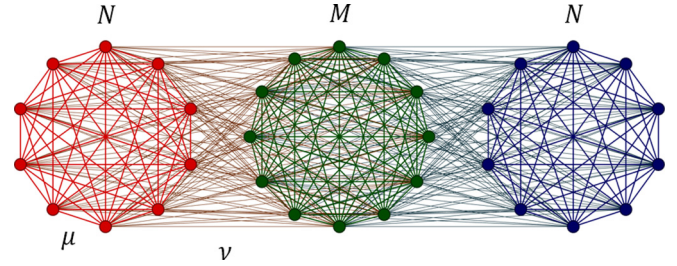


FIG. 1. Three-population network of  $M + 2N$  oscillators (1). Oscillators within each group are all-to-all connected to each other through uniform coupling  $\mu$ . All oscillators in the second group of size  $M$  are connected to all oscillators in the first and third groups of sizes  $N$  through uniform coupling  $\nu$ . There are no direct connections between the first and third groups.

chaotically oscillating and rotating pairwise phase shifts. In particular, we prove the existence of a homoclinic orbit of a saddle-focus fixed point in the 4D system which satisfies the Shilnikov criterion [68] and yields spiral chaos. In Sec. IV, we analyze the variational equations for the stability of the three-cluster pattern as well as of its embedded two-cluster regime where the first and third populations become synchronized between each other, making their phase shift zero. As in the two-population case [60], we derive necessary and sufficient conditions for the constant phase shifts and give bounds on the stability of the cluster patterns with chaotically oscillating and rotating phase shifts. We also discuss the implications of our stability results for the stability of chimeras. Our analytical study is supported by numerical examples which indicate that the three-cluster pattern with chaotic phase shifts may have a fairly large attraction basin and coexist with chimeras and hybrid solitary-chimera states. Section V contains concluding remarks and a discussion. Appendix A provides a nontrivial analysis of the existence of the saddle-focus fixed point. Appendix B gives the proof of the existence of the homoclinic orbit and justifies the parameter space partition into regions with distinct periodic and chaotic intercluster dynamics.

## II. NETWORK MODEL

We consider the three-population network of 2D rotators depicted in Fig. 1 and modeled by the following system:

$$\begin{aligned}
 m\ddot{\theta}_i + \dot{\theta}_i &= \omega_0 + \frac{1}{M + 2N} \left[ \mu \sum_{j=1}^N \sin(\theta_j - \theta_i - \alpha) \right. \\
 &\quad \left. + \nu \sum_{j=1}^M \sin(\phi_j - \theta_i - \alpha) \right], \\
 m\ddot{\phi}_k + \dot{\phi}_k &= \omega_0 + \frac{1}{M + 2N} \left[ \nu \sum_{j=1}^N \sin(\theta_j - \phi_k - \alpha) \right. \\
 &\quad \left. + \mu \sum_{j=1}^M \sin(\phi_j - \phi_k - \alpha) \right. \\
 &\quad \left. + \nu \sum_{j=1}^N \sin(\psi_j - \phi_k - \alpha) \right],
 \end{aligned}$$

$$m\ddot{\psi}_l + \dot{\psi}_l = \omega_0 + \frac{1}{M+2N} \left[ v \sum_{j=1}^M \sin(\phi_j - \psi_l - \alpha) + \mu \sum_{j=1}^N \sin(\psi_j - \psi_l - \alpha) \right], \quad (1)$$

where  $i = 1, \dots, N$ ,  $k = 1, \dots, M$ , and  $l = 1, \dots, N$ . The network is composed of three oscillator populations of sizes  $N$ ,  $M$ , and  $N$ . Variables  $\theta_i$ ,  $\phi_k$ , and  $\psi_l$  correspond to the phases of 2D oscillators from the first, second, and third populations, respectively. The undirected connections within each population are all-to-all with a uniform intragroup coupling  $\mu$ . The oscillators from the second (middle) group of size  $M$  are all-to-all connected to the oscillators from the first and third groups via a uniform intergroup coupling  $v$ . To isolate the effect of adding an extra population to a two-population network, we do not directly couple the first and third groups, thereby introducing a nonglobal structure to the network (1). The oscillators are chosen to be identical, with frequency  $\omega_0$ , phase lag  $\alpha \in [0, \pi/2)$ , and inertia  $m$ . The model (1) is obtained from the Abrams *et al.* chimera model [45,46], consisting of two groups of 1D phase oscillators with Kuramoto-Sakaguchi coupling [36], by increasing the dimension of the phase oscillators, adding the third group, and making the group sizes uneven. The latter property does not allow the network to exhibit complete synchronization, which otherwise could have been the most dominant stable pattern. As a result, the uneven group sizes can promote the emergence of stable clusters.

Introducing new variables  $\tau = \mu t / (M + 2N)$  and  $\beta = \mu m / (M + 2N)$  along with a rotating frame of reference  $\Theta_i = \theta_i - \omega_0 t + c$ ,  $\Phi_k = \phi_k - \omega_0 t + c$ , and  $\Psi_l = \psi_l - \omega_0 t + c$ , where  $c$  is a constant, we can rewrite the system (1) in a more convenient form,

$$\begin{aligned} \beta \ddot{\Theta}_i + \dot{\Theta}_i &= \sum_{j=1}^N \sin(\Theta_j - \Theta_i - \alpha) + \gamma \sum_{j=1}^M \sin(\Phi_j - \Theta_i - \alpha), \\ \beta \ddot{\Phi}_k + \dot{\Phi}_k &= \gamma \sum_{j=1}^N \sin(\Theta_j - \Phi_k - \alpha) \\ &\quad + \sum_{j=1}^M \sin(\Phi_j - \Phi_k - \alpha) \\ &\quad + \gamma \sum_{j=1}^N \sin(\Psi_j - \Phi_k - \alpha), \\ \beta \ddot{\Psi}_l + \dot{\Psi}_l &= \gamma \sum_{j=1}^M \sin(\Phi_j - \Psi_l - \alpha) \\ &\quad + \sum_{j=1}^N \sin(\Psi_j - \Psi_l - \alpha), \end{aligned} \quad (2)$$

where  $\gamma = v/\mu$  represents the ratio between the intra- and intergroup couplings. Without loss of generality, we assume that the intragroup coupling  $\mu$  is stronger than the intergroup coupling  $v$  so that  $\gamma \in (0, 1)$ .

While the network (2) may exhibit various clusters of perfect synchrony induced by additional symmetries of the network connectivity, we will mainly focus on the dynamics and stability of three-group cluster  $C_{\Theta\Phi\Psi}$  where the oscillators are synchronized within the three groups. The existence of this cluster is defined by the invariant manifold (hyperplane)

$$\begin{aligned} C_{\Theta\Phi\Psi} = \{ &\Theta_1 = \dots = \Theta_N = \Theta, \quad \dot{\Theta}_1 = \dots = \dot{\Theta}_N = \dot{\Theta}, \\ &\Phi_1 = \dots = \Phi_M = \Phi, \quad \dot{\Phi}_1 = \dots = \dot{\Phi}_M = \dot{\Phi}, \\ &\Psi_1 = \dots = \Psi_N = \Psi, \quad \dot{\Psi}_1 = \dots = \dot{\Psi}_N = \dot{\Psi} \}. \end{aligned} \quad (3)$$

Hereafter, we will refer to  $C_{\Theta\Phi\Psi}$  as a ‘‘manifold’’ or a ‘‘solution’’ interchangeably, depending on what term is more suitable in a particular context.

Notice that the equal node degree is a necessary condition for oscillators to form a synchronous cluster. Therefore, the oscillators from the second group of size  $M$  may not be synchronized with the oscillators from the first and third groups of size  $N$ , whereas the latter can form a cluster. As a result, the three-group cluster manifold  $C_{\Theta\Phi\Psi}$  has an embedded invariant two-cluster manifold,

$$\begin{aligned} C_{\Theta\Phi\Theta} = \{ &\Theta_1 = \dots = \Theta_N = \Theta, \quad \dot{\Theta}_1 = \dots = \dot{\Theta}_N = \dot{\Theta}, \\ &\Phi_1 = \dots = \Phi_M = \Phi, \quad \dot{\Phi}_1 = \dots = \dot{\Phi}_M = \dot{\Phi}, \\ &\Psi_1 = \dots = \Psi_N = \Theta, \quad \dot{\Psi}_1 = \dots = \dot{\Psi}_N = \dot{\Theta} \}, \end{aligned} \quad (4)$$

which represents the largest possible cluster partition of the network (2) with one synchronous cluster composed of all oscillators from the first and third groups and the other formed by all oscillators from the second group.

In the following, we will analyze the dynamics and stability of synchronous clusters  $C_{\Theta\Phi\Psi}$  and  $C_{\Theta\Phi\Theta}$  and reveal the role of the intrinsic oscillator parameters, coupling strength, and network sizes in controlling the onset of each of the two cluster regimes.

### III. POSSIBLE INTERCLUSTER DYNAMICS

We first study the existence of possible temporal dynamics in the three-cluster manifold  $C_{\Theta\Phi\Psi}$ . These dynamics are described by the following system obtained from system (2) by removing the indexes  $i, j, k$ :

$$\begin{aligned} \beta \ddot{\Theta} + \dot{\Theta} &= \gamma M \sin(\Phi - \Theta - \alpha) - N \sin \alpha, \\ \beta \ddot{\Phi} + \dot{\Phi} &= \gamma N [\sin(\Theta - \Phi - \alpha) + \sin(\Psi - \Phi - \alpha)] \\ &\quad - M \sin \alpha, \\ \beta \ddot{\Psi} + \dot{\Psi} &= \gamma M \sin(\Phi - \Psi - \alpha) - N \sin \alpha. \end{aligned} \quad (5)$$

Introducing the differences between the phases  $x = \Theta - \Phi$  and  $z = \Psi - \Phi$ , we obtain the equations that govern the dynamics of the phase differences between the

clusters

$$\begin{aligned}\beta\ddot{x} + \dot{x} &= (M - N) \sin \alpha - \gamma[N \sin(x - \alpha) \\ &\quad + M \sin(x + \alpha) + N \sin(z - \alpha)], \\ \beta\ddot{z} + \dot{z} &= (M - N) \sin \alpha - \gamma[N \sin(x - \alpha) \\ &\quad + M \sin(z + \alpha) + N \sin(z - \alpha)].\end{aligned}\quad (6)$$

### A. Transformation to coupled pendulum equations

Like in [60], we set  $\Omega = (M - N) \sin \alpha$ ,  $R = \gamma \sqrt{N^2 + M^2 + 2MN \cos 2\alpha}$ , and  $\delta_0 = \arctan\left(\frac{M-N}{M+N} \tan \alpha\right)$  and use trigonometric formulas to turn the system (6) into

$$\begin{aligned}\beta\ddot{x} + \dot{x} &= \Omega - R \sin(x + \delta_0) - \gamma N \sin(z - \alpha), \\ \beta\ddot{z} + \dot{z} &= \Omega - R \sin(z + \delta_0) - \gamma N \sin(x - \alpha).\end{aligned}\quad (7)$$

Shifting the variables  $(x, z) \rightarrow (x + \delta_0, z + \delta_0)$ , setting  $\delta = \alpha + \delta_0$ , and rescaling time  $\tau = t \sqrt{\frac{\beta}{R}}$ , we obtain

$$\begin{aligned}\ddot{x} + h\dot{x} + \sin x &= \omega - a \sin(z - \delta), \\ \ddot{z} + h\dot{z} + \sin z &= \omega - a \sin(x - \delta),\end{aligned}\quad (8)$$

where  $h = \frac{1}{\sqrt{\beta R}}$ ,  $\omega = \frac{\Omega}{R}$ ,  $a = \frac{\gamma N}{R}$ ,  $\dot{x} = \frac{dx}{d\tau}$ , and  $\dot{z} = \frac{dz}{d\tau}$ . Observe that (8) is a 4D system of two coupled pendulums and therefore can exhibit complex dynamics. In some sense, each pendulum equation of (8) may also be viewed as a periodically driven nonlinear pendulum which is notoriously known for its chaotic behavior [69].

### B. Fixed points

Depending on the parameters, the 4D system (8) may have up to four fixed points such that each point  $(x^*, z^*)$  corresponds to a constant phase shift  $x^*$  ( $z^*$ ) between the first (third) and second clusters. In the following, we will show that two out of the four fixed points may be saddle foci with a positive saddle value which can undergo a homoclinic bifurcation and induce Shilnikov-type chaotic intercluster dynamics.

System (8) is symmetric in  $x$  and  $z$  and has an invariant manifold  $x = z$  which corresponds to the cluster manifold  $C_{\Theta\Phi\Theta}$ . The dynamics on the manifold  $C_{\Theta\Phi\Theta} : \{x = z\}$  is described by the system

$$\ddot{x} + h\dot{x} + \sin x + a \sin(x - \delta) = \omega,$$

which can be further reduced to a pendulum equation by combining the sine terms and using a trigonometric identity so that

$$\ddot{x} + h\dot{x} + a_1 \sin(x - \delta_1) = \omega, \quad (9)$$

where  $a_1 = \sqrt{1 + a^2 + 2a \cos \delta}$  and  $\delta_1 = \arctan \frac{a \sin \delta}{1 + a \cos \delta}$ .

Therefore, for  $\omega < a_1$ , the 4D system (8) has two fixed points,

$$\begin{aligned}O_1 &\left(x_s = z_s = \arcsin \frac{\omega}{a_1} + \delta_1\right), \\ O_2 &\left(x_u = z_u = \pi - \arcsin \frac{\omega}{a_1} + \delta_1\right),\end{aligned}\quad (10)$$

which belong to  $C_{\Theta\Phi\Theta}$ . The type and stability of these fixed points along the cluster manifold  $C_{\Theta\Phi\Theta}$  are defined through

(9), whose dynamics are similar to the classical pendulum equation with a constant torque  $\omega$  [70]. Therefore,  $O_1$  ( $O_2$ ) is a stable (saddle) fixed point with respect to the dynamics restricted to  $C_{\Theta\Phi\Theta}$ . While the directions transversal to  $C_{\Theta\Phi\Theta}$  may be unstable, depending on the parameters of system (8), the fixed point  $O_1$  ( $O_2$ ) may become a saddle node (a saddle). As in the classical pendulum equation [70], these fixed points disappear via a saddle-node bifurcation in system (9) at  $\omega = a_1$ .

System (8) also has two other fixed points that belong to the three-cluster manifold  $C_{\Theta\Phi\Psi}$  but lie outside the manifold  $C_{\Theta\Phi\Theta}$  so that  $x \neq z$ . These fixed points  $O_3(x_3, z_3)$  and  $O_4(x_4, z_4)$  have the coordinates

$$\begin{aligned}x_{3,4} &= \arctan\left(\frac{1 - a \cos \delta}{a \sin \delta}\right) \\ &\quad \pm \arccos\left(\frac{\omega \sqrt{1 + a^2 - 2a \cos \delta}}{1 - a^2}\right), \\ z_{3,4} &= \arctan\left(\frac{1 - a \cos \delta}{a \sin \delta}\right) \\ &\quad \mp \arccos\left(\frac{\omega \sqrt{1 + a^2 - 2a \cos \delta}}{1 - a^2}\right).\end{aligned}\quad (11)$$

The derivation of the fixed points' coordinates is given in Appendix A.

The stability of fixed points  $O_1$ ,  $O_2$ ,  $O_3$ ,  $O_4$  of system (8) can be evaluated through the characteristic equation

$$\begin{aligned}(s^2 + hs + \cos x^*)(s^2 + hs + \cos z^*) \\ - a^2 \cos(x^* - \delta) \cos(z^* - \delta) = 0,\end{aligned}\quad (12)$$

where  $x^*$  and  $z^*$  are the coordinates of the fixed point in question [see (10) and (11)]. The derivation of general close-form solutions for the fourth-order polynomial equation (12) might require the use of symbolic computations or even be out of reach. Here, we take a different route towards placing explicit bounds on the parameters of system (8) which guarantee that points  $O_3$  and  $O_4$  are saddle foci with a positive saddle value. To do so, we set

$$\lambda = s^2 + hs \quad (13)$$

to turn (12) into the biquadratic equation

$$\begin{aligned}\lambda^2 + (\cos x^* + \cos z^*)\lambda + \cos x^* \cos z^* \\ - a^2 \cos(x^* - \delta) \cos(z^* - \delta) = 0.\end{aligned}\quad (14)$$

Its roots are

$$\begin{aligned}\lambda_{1,2} &= \frac{1}{2}[-\cos x^* - \cos z^* \\ &\quad \pm \sqrt{(\cos x^* + \cos z^*)^2 + 4a^2 \cos(x^* - \delta) \cos(z^* - \delta)}].\end{aligned}\quad (15)$$

Towards our goal of obtaining sufficient conditions that guarantee that points  $O_3$  and  $O_4$  are saddle foci, we assume that the discriminant of (15) is positive. Note that this assumption can be realized by choosing appropriate values of  $\gamma$  and  $\omega$  which can change  $x^*$  and  $z^*$  accordingly while keeping  $\delta$  intact. It follows from this assumption that  $\lambda_1 > 0$  and  $\lambda_2 < 0$ . Thus,

substituting constants (15) into (13), we obtain a quadratic equation whose solutions are

$$s_{11,12} = -\frac{h}{2} \pm \sqrt{\frac{h^2}{4} + \lambda_1}, \quad s_{21,22} = -\frac{h}{2} \pm i\sqrt{\left|\frac{h^2}{4} + \lambda_2\right|}, \quad (16)$$

where  $s_{21,22}$  are complex when  $|\lambda_2| > h^2/4$ . Therefore, under these conditions, the fixed point  $O_3$  ( $O_4$ ) is a saddle focus with the 1D unstable manifold corresponding to the positive eigenvalue  $s_{11} = -\frac{h}{2} + \sqrt{\frac{h^2}{4} + \lambda_1}$  and the 3D stable manifold composed of the 2D stable focus manifold which is determined by the complex eigenvalues  $s_{21,22}$  and the 1D stable manifold defined by the negative eigenvalue  $s_{12}$ . These saddle foci  $O_3$  and  $O_4$  have a positive saddle value [68]  $\sigma = \text{Re}(s_{21,22}) + s_{11} > 0$  if  $\lambda_1 > \frac{3}{4}h^2$ . Therefore, the saddle foci  $O_3$  and  $O_4$  satisfy the Shilnikov criterion for spiral chaos [68] which emerges as a result of a Shilnikov homoclinic bifurcation. In the following, we will derive sufficient conditions for the parameters of system (8) under which fixed points  $O_3$  and  $O_4$  can undergo homoclinic bifurcations leading to chaotic intercluster dynamics.

### C. Oscillatory, rotatory, and mixed-mode phase shifts

In addition to the fixed points which, when stable, induce constant intercluster phase shifts  $x$  and  $z$ , system (8) may have three main types of nontrivial, possibly chaotic, dynamics such as (i) oscillatory trajectories which do not rotate around the cylinder projection  $(x, \dot{x})$  or  $(z, \dot{z})$  and are centered around the fixed point  $O_1$ , (ii) rotatory trajectories that encircle the cylinder projection  $(x, \dot{x})$  or  $(z, \dot{z})$ , similar to the limit cycle of a rotatory type in the classical pendulum equation (17), and (iii) mixed-mode trajectories that make several oscillatory turns while traveling around the cylinder. Note that this classification distinguishes between the motions along the  $(x, \dot{x})$  and  $(z, \dot{z})$  projections so each phase shift  $x$  or  $z$  may individually exhibit oscillatory, rotatory, or mixed-mode dynamics. As a result, the relative evolution of  $x$  and  $z$  may be a combination of the three dynamics, yielding oscillating-oscillating, oscillating-rotating, rotating-rotating, mixed-mode-oscillating, or mixed-mode-rotating phase shifts. In this classification, the term oscillating-rotating refers to the case where the phase shift  $x$  oscillates around the fixed point with a small amplitude, whereas the phase shift  $z$  rotates from 0 to  $2\pi$  around the cylinder. This classification can also be extended to incorporate the coexistence of constant and time-varying shifts. While a complete analytical study of possible dynamics of 4D system (8) is complicated and may be out of reach, we adapt the auxiliary system method [71] to derive bounds that single out regions of parameters with possible homoclinic bifurcations of the fixed points and oscillatory, rotatory, and mixed-mode phase shifts.

*Statement 1. Sufficient conditions.* Consider the partition of the  $(h, \omega)$  parameter space of system (8) shown in Fig. 2. Let  $T(h)$  denote the Tricomi homoclinic curve [72] of the pendulum equation

$$\ddot{x} + h\dot{x} + \sin x = \omega, \quad (17)$$

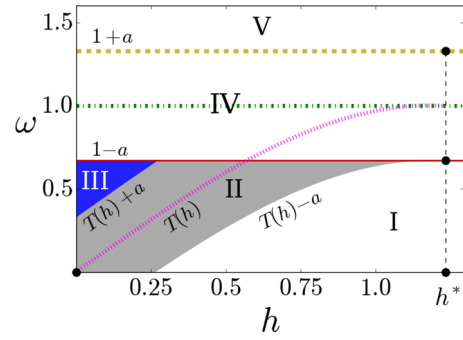


FIG. 2. Existence diagram for possible phase shift dynamics in system (8) (an illustration of Statement 1). Region I [ $\omega < T(h) - a$ ]: Only constant or oscillating phase shifts  $x(t)$  and  $z(t)$ . Region II (light gray): Possible coexistence of constant, oscillating, rotating, and mixed-mode phase shifts. Homoclinic bifurcations of fixed points  $O_3$  and  $O_4$  take place only in this region. Region III (blue): The coexistence of the phase shifts of all three types is guaranteed. Region IV ( $1 - a < \omega < 1 + a$ ): Possible coexistence of oscillating, rotating, and phase shifts. Region V ( $\omega > 1 + a$ ): Only rotating phase shifts are possible.  $T(h)$  is the Tricomi homoclinic curve (18) of pendulum equation (17) (pink dashed line). Damping  $h = \frac{1}{\sqrt{\beta R}}$ , where  $R = \gamma\sqrt{N^2 + M^2} + 2MN \cos 2\alpha$ . Fixed parameters are  $M = 12$ ,  $N = 5$ ,  $\gamma = 0.4$ , and  $\alpha = \pi/6$ .

which can be approximated as in [60] by

$$\omega = T(h) \approx \begin{cases} \frac{4}{\pi}h - 0.305h^3 & \text{for } 0 < h < h^* \approx 1.22, \\ 1 & \text{for } h > h^*. \end{cases} \quad (18)$$

Then five regions of the parameter partition correspond to the following dynamics of system (8).

(1) *Region I:*  $\omega < T(h) - a$ . Only oscillatory trajectories that do not encircle the cylinder projections  $(x, \dot{x})$  and  $(z, \dot{z})$  are permissible.

(2) *Region II:*  $\{\omega < 1 - a\} \cap \{\omega < T(h) + a\} \cap \{\omega > T(h) - a\}$ . Fixed points  $O_3$  and  $O_4$  of system (8) undergo homoclinic bifurcations only in this region. Oscillatory, rotatory, and mixed-mode trajectories are possible.

(3) *Region III:*  $T(h) + a < \omega < 1 - a$ . The coexistence of oscillatory and rotatory trajectories is guaranteed. Mixed-mode oscillations are impossible.

(4) *Region IV:*  $1 - a < \omega < 1 + a$ . Trajectories of all three types are possible, with the prevalence of rotatory and mixed-mode phase shift trajectories.

(5) *Region V:*  $\omega > 1 + a$ . Only rotatory trajectories that encircle the cylinder projections  $(x, \dot{x})$  and  $(z, \dot{z})$  are possible.

*Proof.* The proof is given in Appendix B. ■

Figure 3 relates these regions of parameters  $h$  and  $\omega$  to the original parameters of network (2). Hereafter, we choose the phase lag  $\alpha$  and inertia  $\beta$  as control parameters and fix the group sizes  $N = 24$  and  $M = 25$  and the ratio between the intra- and intergroup coupling  $\gamma = 0.4$ . We aim to show that even a minimal difference between the sizes of the first (third) group of  $N$  oscillators and the second group of  $M$  oscillators can yield phase shift chaos. In this case, the  $(h, \omega)$  diagram of Fig. 2 typically does not contain region III as the curve  $\omega = T(h) + a$  is located above the line  $\omega = 1 - a$ . Recast in

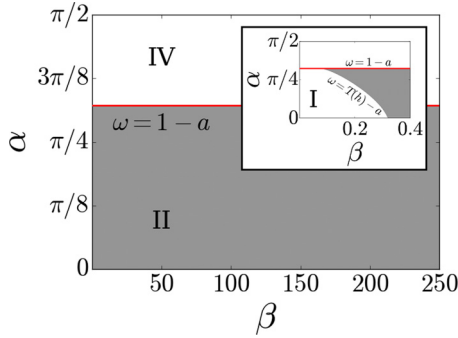


FIG. 3. Existence diagram of Fig. 2 recast into the original parameters  $\alpha$  and  $\beta$  of system (2) for  $M = 25$ ,  $N = 24$ , and  $\gamma = 0.4$ . Only regions I, II, and IV are present. The red line corresponds to the curve  $\omega = 1 - a$  in Fig. 2. The inset shows the region of small values of  $\beta$  where region I exists.

parameters  $\alpha$  and  $\beta$ , this diagram typically maximizes the size of regions II and IV and minimizes region I over a large range of inertia  $\beta$  (see Fig. 3).

The parameter partition in Fig. 2 characterizes the regions of parameters where different types of phase shifts are possible and where homoclinic bifurcations of  $O_3$  and  $O_4$  leading to the emergence of chaotic dynamics take place. More specifically, in region I, the phase shifts  $x(t)$  and  $z(t)$  may only be constant or may periodically or chaotically oscillate with a small amplitude. Region II corresponds to the richest dynamics where all three types of time-varying phase shifts are possible, thereby allowing for oscillatory, rotatory, and mixed-mode chaos. In this region,  $O_3$  and  $O_4$  undergo homoclinic bifurcations, yielding Shilnikov spiral chaos. While chaotic shift dynamics may be observed in the other regions of the parameter partition, this spiral chaos originates from region II due to the homoclinic bifurcations and persists beyond this region. The dynamics in region III are similar to those in region II, except that the coexistence of oscillating, rotating, and mixed-mode phase shifts is guaranteed by Statement 1. Region IV represents a transition zone, where, similar to regions II and III, all three types of time-varying phase shifts may appear. However, the rotatory phase shifts become more frequent as  $\omega$  increases toward  $\omega = 1 + a$ , finally entering into region V, where only rotatory phase shifts are possible.

To support our analytical analysis and prediction, we have numerically studied the dynamics of phase shifts in system (8) (see Fig. 4) and found regions of parameters which yield chaotic mixed-mode–mixed-mode (sample point A, Fig. 5), rotating-rotating (sample point B, Fig. 6), and rotating-oscillating (sample point C, Fig. 7) phase shift regimes. As expected, a majority of the chaotic regions lie in region II (compare Figs. 4 and 3), where homoclinic bifurcations of fixed points  $O_3$  and  $O_4$  give birth to spiral chaos. A detailed analysis of these homoclinic bifurcations and transitions to chaos is beyond the scope of this paper and will be reported elsewhere. However, we have verified the eigenvalues of fixed points  $O_3$  and  $O_4$  at sample points A, B, and C. These eigenvalues are identical for both  $O_3$  and  $O_4$  due to the symmetries of (11) and (12). For the parameters corresponding to sample points

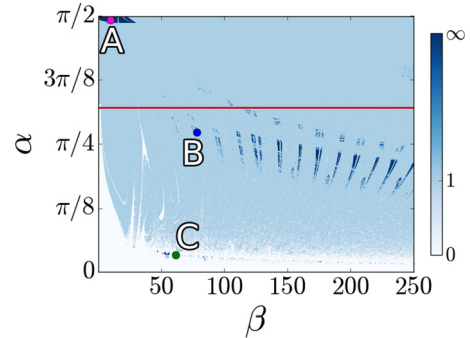


FIG. 4. Regular and chaotic phase shift dynamics of system (8) evaluated numerically as a function of parameters  $\alpha$  and  $\beta$ . The color coding corresponds to the period of a limit cycle. White regions correspond to fixed points with a zero winding number; light blue regions correspond to a winding number of 1 (period-1 limit cycles); dark blue regions correspond to chaotic orbits with infinitely large winding numbers. Sample points A, with  $(\beta, \alpha) = (10, 397\pi/800)$ ; B, with  $(\beta, \alpha) = (78.125, 437\pi/1600)$ ; and C, with  $(\beta, \alpha) = (61.5625, 27\pi/800)$ , correspond to chaotic mixed-mode–mixed-mode, rotating-rotating, and oscillating-rotating phase shift regimes, respectively (see Figs. 5–7). The red horizontal line corresponds to the line  $\omega = 1 - a$  in Fig. 3. The region under the red line is region II, where homoclinic bifurcations give birth to chaos. Other parameters are as in Fig. 3.

B and C, the eigenvalues satisfy the assumption that  $\lambda_1 > 0$  and  $\lambda_2 < 0$  [see (15)] and therefore can be calculated analytically through (16). This yields the eigenvalues  $s_{11} = 0.7499$ ,  $s_{12} = -0.7815$ , and  $s_{21,22} = -0.0158 \pm 0.8609i$  (for sample point B) and  $s_{11} = 0.9184$ ,  $s_{21} = -0.9472$ , and  $s_{21,22} = -0.0144 \pm 0.9330i$  (for sample point C). Thus, fixed points  $O_3$  and  $O_4$  are saddle foci with a positive saddle value  $\sigma$  and have 1D unstable and 3D stable manifolds. As a result,  $O_3$  and  $O_4$  satisfy the Shilnikov criterion [73] and offer a possible mechanism for the emergence of different forms of spiral chaos in system (8) and, ultimately, in the three-group network (2). In particular, Fig. 7, corresponding to sample point C, demonstrates the existence of a representative spiral chaotic regime where the phase shift  $x(t)$  between the first and second groups of synchronized oscillators in network (2) rotates chaotically between  $-\pi$  and  $\pi$ , whereas the phase shift  $z(t)$  oscillates chaotically within a smaller range of  $z(t) \in (-1.0, 1.0)$ .

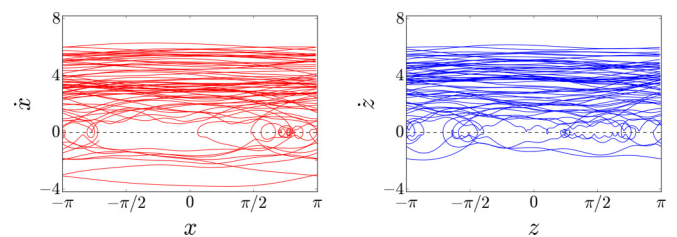


FIG. 5. Mixed-mode–mixed-mode phase shift regime corresponding to point A in Fig. 4. Both  $x$  and  $z$  phase shifts are of mixed-mode type with the prevalence of chaotic rotatory motions. The values of  $x$  and  $z$  are projected onto a flattened cylinder where  $x \rightarrow (x - \pi) \bmod (2\pi) - \pi$  and  $z \rightarrow (z - \pi) \bmod (2\pi) - \pi$ .

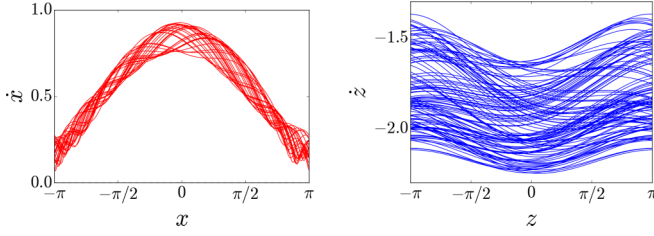


FIG. 6. Rotating-rotating phase shift regime corresponding to point *B* in Fig. 4. Both *x* and *z* phase shifts chaotically rotate around the cylinder.

#### IV. STABILITY ANALYSIS

Having studied the existence of possible phase shift regimes between the synchronized groups defined by the cluster manifold  $C_{\Theta\Phi\Psi}$ , we proceed with a stability analysis which indicates what phase shifts can stably emerge in the network.

##### A. Stability of the three-cluster manifold $C_{\Theta\Phi\Psi}$

To determine the conditions under which the synchronous three-group cluster with constant, periodic, or chaotic shifts  $x(t)$  and  $z(t)$  can stably emerge in the network, we linearize system (2) about the synchronous cluster solution

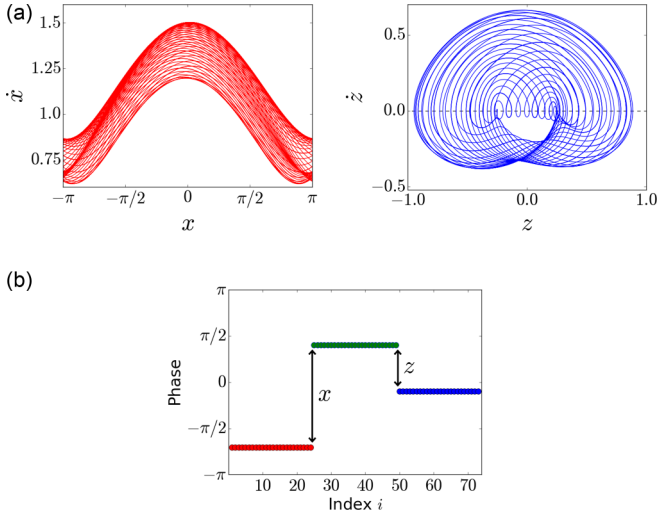


FIG. 7. (a). Rotating-oscillating phase shift regime corresponding to point *C* in Fig. 4. The *x* and *z* phase shifts exhibit rotatory and oscillatory chaos, respectively. (b) Snapshot of the corresponding three-cluster pattern in network (2) of  $M + 2N$  oscillators with  $M = 25$  and  $N = 24$ . The initial states are chosen on the manifold  $C_{\Theta\Phi\Psi}$  to form the corresponding three clusters where the colored dot indicates the instantaneous phase of oscillator with index *i*. The initial conditions for  $x(t)$  and  $z(t)$  are chosen randomly from (0,1). The rotating phase shift between the first (red dots) and second (green dots) clusters is governed by  $x(t)$  and makes large chaotic excursions between  $-\pi$  and  $\pi$ . The oscillating phase shift between the second (green dots) and third (blue dots) clusters is driven by  $z(t)$  and therefore oscillates between  $-1$  and  $1$ .

$C_{\Theta\Phi\Psi} : \{\Theta, \dot{\Theta}, \Phi, \dot{\Phi}, \Psi, \dot{\Psi}\}$ . This yields

$$\begin{aligned} \beta \ddot{\xi}_i + \dot{\xi}_i &= -q_1 + \cos \alpha \sum_{j=1}^N \xi_j + \gamma \cos(x + \alpha) \sum_{j=1}^M \eta_j, \\ \beta \dot{\eta}_k + \dot{\eta}_k &= -q_2 \eta_k + \cos \alpha \sum_{j=1}^M \eta_j + \gamma \cos(x - \alpha) \sum_{j=1}^N \xi_j \\ &\quad + \gamma \cos(z - \alpha) \sum_{j=1}^N \xi_j, \\ \beta \ddot{\zeta}_l + \dot{\zeta}_l &= -q_3 \zeta_l + \cos \alpha \sum_{j=1}^N \zeta_j + \gamma \cos(z + \alpha) \sum_{j=1}^M \eta_j, \end{aligned} \quad (19)$$

where  $\xi_i$ ,  $i = 1, \dots, N$ ;  $\eta_k$ ,  $k = 1, \dots, M$ ; and  $\zeta_l$ ,  $l = 1, \dots, N$  are infinitesimal perturbations of the *i*th oscillator's synchronous solution  $\Theta$ ,  $\Phi$ ,  $\Psi$ , respectively, and

$$q_1 = N \cos \alpha + \gamma M \cos(x + \alpha), \quad (20a)$$

$$q_2 = M \cos \alpha + \gamma N [\cos(x - \alpha) + \cos(z - \alpha)], \quad (20b)$$

$$q_3 = N \cos \alpha + \gamma M \cos(z + \alpha). \quad (20c)$$

Hereafter, we go back to the original notations  $x = \Theta - \Phi$  and  $z = \Psi - \Phi$ , which differ from the shifted variables  $x$  and  $z$ , used in system (8) and in the remainder of Sec. III, by the constant  $\delta_0$ . This abuse of notation simplifies the exposition as  $x$  and  $z$  always denote the phase shifts between the cluster groups. At the same time, the use of the original notations makes the stability analysis more manageable and leads to stability conditions which are easier to express in terms of the original parameters of network model (2).

In a manner similar to [60], we study the transversal stability of  $C_{\Theta\Phi\Psi}$  by introducing the difference variables

$$\begin{aligned} s_i &= \xi_i - \xi_{i+1}, \quad i = 1, \dots, N - 1, \\ u_k &= \eta_k - \eta_{k+1}, \quad k = 1, \dots, M - 1, \\ w_\ell &= \zeta_\ell - \zeta_{\ell+1}, \quad \ell = 1, \dots, N - 1 \end{aligned} \quad (21)$$

and subtracting the corresponding equations in (19) to obtain

$$\beta \ddot{s}_i + \dot{s}_i + q_1 s_i = 0, \quad i = 1, \dots, N, \quad (22a)$$

$$\beta \ddot{u}_k + \dot{u}_k + q_2 u_k = 0, \quad k = 1, \dots, M, \quad (22b)$$

$$\beta \ddot{w}_l + \dot{w}_l + q_3 w_l = 0, \quad l = 1, \dots, N. \quad (22c)$$

Here, the sum terms from (19) have collapsed into  $q_1$ ,  $q_2$ , and  $q_3$  due to the symmetry of the global intra- and intercluster coupling, thereby decoupling Eqs. (22a)–(22c) and significantly simplifying their stability analysis.

The linearized equations (22a)–(22c) are governed by the phase shifts  $x$  and  $z$  through (7). Therefore, in the simple case where  $x_e = x_s - \delta_0$  and  $z_e = z_s - \delta_0$  are constant and determined by fixed point  $O_1(x_s, z_s)$  when it exists and is stable, the analysis of (22a)–(22c) amounts to evaluating the signs of  $q_1$ ,  $q_2$ , and  $q_3$  at  $x_e, z_e$ . Hence, the stability of (22a)–(22c) is guaranteed iff

$$q_{1,2,3}|_{x_e, z_e} > 0. \quad (23)$$

This claim can be easily checked by looking at the characteristic equations  $\beta p^2 + p + q_{1,2,3} = 0$  for the linear differential equations (22a)–(22c) with constant coefficients. Here,  $q_{1,2,3}$  must be positive for the real parts of the characteristic equations to be negative.

The criterion (23) represents the necessary and sufficient condition for the stability of the synchronous cluster solution  $C_{\Theta\Phi\Psi}$  with constant phase shifts  $x_e$  and  $z_e$  and can be easily applied as long as the fixed point  $O_1$  exists for  $\omega < a_1$ .

In the more complex case where the phase shifts  $x_s$  and  $z_s$  are time-varying, the linear equations (22a)–(22c) contain time-dependent coefficients  $q_1, q_2, q_3$ . Therefore, the exact stability conditions of (22a)–(22c) can be obtained numerically only by calculating the Lyapunov exponents. However, we manage to analytically derive sufficient conditions which guarantee that the cluster solution  $C_{\Theta\Phi\Psi}$  with even chaotic phase shifts  $x(t)$  and  $z(t)$  is locally stable. This leads to the following assertion.

*Statement 2. Sufficient conditions.* The cluster solution  $C_{\Theta\Phi\Psi}$  with oscillating or rotating phase shifts  $x(t)$  and  $z(t)$  is locally stable in the transversal direction if

$$\sqrt{2}\gamma < \cos \alpha < \min \left\{ \frac{1 - 4\beta\gamma M}{4\beta N}, \frac{1 - 8\beta\gamma N}{4\beta M} \right\}. \quad (24)$$

*Proof.* Since the coefficients  $q_1(t)$ ,  $q_2(t)$ , and  $q_3(t)$  become time-dependent when the phase shifts  $x(t)$  and  $z(t)$  vary in time, the stability condition (23) for the variational equations (22a)–(22c) is no longer sufficient. To derive such a sufficient condition, we use the stability criterion [74] which guarantees that a linear second-order equation with a time-varying coefficient  $q(t)$

$$\beta \ddot{v} + \dot{v} + q(t)v = 0 \quad (25)$$

is stable if

$$q(t) > 0, \quad (26a)$$

$$D(t) = 1 - 4\beta q(t) > 0 \quad \forall t, \quad (26b)$$

where  $D(t)$  is the discriminant of the characteristic equation  $\beta p^2 + p + q(t) = 0$  with the frozen time  $t$ . In other words, this conservative criterion guarantees that the linear equation (25) with time-varying coefficient  $q(t)$  is stable as long as the fixed point  $v = 0$  is a stable node for any  $t > 0$  and never becomes a stable focus or a degenerate node.

Applying the criterion (26a) and (26b) to the variational equations (20a)–(20c), we first verify the condition (26a) for  $q_1(t)$ ,  $q_2(t)$ , and  $q_3(t)$ . To impose that conservative conditions on  $q_{1,2,3}$  are positive, we consider the worst-case bounds which minimize  $q_{1,2,3}$  in (20a)–(20c):

$$\begin{aligned} \cos[x(t) + \alpha] &= -1, & \cos[x(t) - \alpha] &= -1, \\ \cos[z(t) - \alpha] &= -1, & \cos[z(t) + \alpha] &= -1. \end{aligned} \quad (27)$$

This implies that

$$q_{1,3}(t) > 0 \quad \forall t \text{ if } \cos \alpha > \gamma M/N, \quad (28a)$$

$$q_2(t) > 0 \quad \forall t \text{ if } \cos \alpha > 2\gamma N/M. \quad (28b)$$

Solving the inequality in (28a) for  $N/M$  and then substituting  $N/M = \gamma/\cos \alpha$  into (28b), we obtain the condition that

guarantees that  $q_{1,2,3} > 0$  for any  $t$  if

$$\cos \alpha > \sqrt{2}\gamma. \quad (29)$$

This bound yields the left-hand side part of inequality (24).

Finally, to verify the condition (26b) for discriminants  $D_{1,2,3}(t)$  to be positive for (20a)–(20c), we consider the worst-case scenario bounds which maximize  $q_{1,2,3}$ . These are the conditions (27) with  $-1$  replaced with  $+1$ . Thus, the condition (26b) is satisfied for (20a)–(20c) for any time  $t > 0$  if

$$4\beta(N \cos \alpha + \gamma M) < 1, \quad 4\beta(M \cos \alpha + 2\gamma N) < 1. \quad (30)$$

Solving (30) for  $\cos \alpha$  and choosing the lowest of the two bounds yields the right-hand side part of the inequality (24). ■

*Remark 1.* If the sizes of the cluster groups are such that  $2N > M$  (as in the numerical examples of Figs. 3–7), then the condition (24) becomes

$$\sqrt{2}\gamma < \cos \alpha < \frac{1 - 8\beta\gamma N}{4\beta M}, \quad (31)$$

as this right-hand side bound is always the minimum of the two in (24).

*Remark 2.* The bound (24) is very conservative due to the use of the worst-case stability conditions. Therefore, it should be considered a proof of concept that analytically demonstrates that the cluster solution  $C_{\Theta\Phi\Psi}$  with time-varying, possibly chaotic, phase shifts  $x(t)$  and  $z(t)$  can be stable. Moreover, this stability condition clearly reveals a destabilizing role of the inertia  $\beta$  in the stability of  $C_{\Theta\Phi\Psi}$ . Indeed, increasing  $\beta$  reduces the right-hand side of inequality (24) and therefore diminishes the range of  $\alpha$  in which the cluster solution is stable, thereby eventually making the cluster solution unstable for higher  $\beta$  [see Fig. 8 for the actual stability regions revealed via numerical simulations and Fig. 9 for the comparison with the conservative bound (24)].

Figure 8 demonstrates stability diagrams for synchronization of the oscillators within each of the three groups, evaluated via the Kuramoto order parameter  $r = \frac{1}{n} \sum_{j=1}^n \langle e^{i\varphi_j} \rangle$ , calculated separately for the phases within the first ( $\varphi_j = \Theta_j$ ,  $j = 1, \dots, N$ ), second ( $\varphi_j = \Phi_j$ ,  $j = 1, \dots, M$ ), and third ( $\varphi_j = \Psi_j$ ,  $j = 1, \dots, N$ ) groups, where  $\langle \dots \rangle$  denotes a time average. Notice that the three-cluster solution  $C_{\Theta\Phi\Psi}$  with the mixed-mode–mixed-mode chaotic shifts depicted in Fig. 5 and corresponding to point A in the existence (Fig. 4) and stability (Fig. 8) diagrams is unstable. This is in qualitative agreement with the sufficient condition of Statement 2, which predicts a general tendency of an increased phase lag parameter  $\alpha \in [0, \pi/2)$  to hinder the stability of the cluster solution via decreasing  $\cos \alpha$  in (24). In fact, point A is located in a region of  $\alpha$  close to  $\pi/2$ , where  $\cos \alpha$  is close to zero, thereby making the stability conditions (26a) and (26b) impossible to satisfy. At the same time, lower values of  $\alpha$  yield the stability of the three-cluster solution with the rotating-rotating and rotating-oscillating chaotic phase shifts, corresponding to points B and C, respectively.

Recall that the analytical stability conditions (26a) and (26b) are applied to each of  $q_1(t)$ ,  $q_2(t)$ , and  $q_3(t)$  to guarantee the stability of the uncoupled variational equations (22a), (22b), and (22c), respectively. Therefore, when the conditions (26a) and (26b) are violated for  $q_2$  while remaining valid for  $q_1$  and  $q_3$ , the trivial fixed point of the variational equations

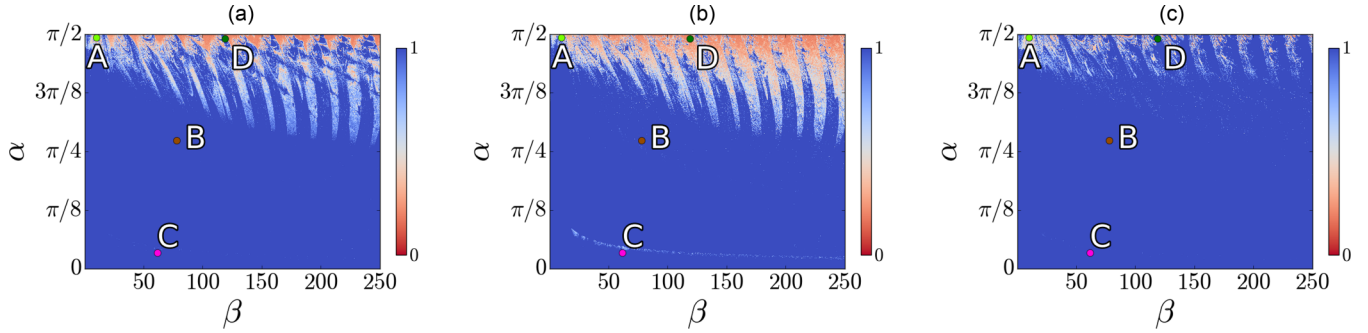


FIG. 8. Numerical stability diagrams for synchronization within the (a) first, (b) second, and (c) third groups of oscillators. The color bar indicates the Kuramoto order parameter  $r$  calculated for the oscillators' phases within each group. The blue regions with  $r = 1$  indicate synchronization within the corresponding group. Points  $A, B, C$  correspond to sample points  $A, B, C$  from the existence diagram of Fig. 4. Point  $A$  lies in the instability (red) zones of all three diagrams, rendering the cluster manifold  $C_{\Theta\Phi\Psi}$  unstable. Points  $B$  and  $C$  correspond to a stable  $C_{\Theta\Phi\Psi}$ . Notice point  $D$  with  $\alpha = 49\pi/100$  and  $\beta = 475/4$ , which lies in the stability (blue) regions of diagrams (a) and (c) and in the instability (red) region of diagram (b), thereby corresponding to a one-headed chimera (see Fig. 10). Initial conditions are chosen close to the cluster manifold  $C_{\Theta\Phi\Psi}$  (see the text for the details). Parameters are as in Fig. 4.

(22a)–(22c) can become a saddle. In this case, this saddle fixed point can yield a *chimera state*, in which the oscillators within the first and third groups of size  $N$  may remain synchronized [as the conditions (26a) and (26b) for  $q_1$  and  $q_3$  are satisfied], while the oscillators from the second group of size  $M$  form an incoherent state. The numerical stability diagrams of Fig. 8 indicate that the instability region is the largest for the second cluster [see Fig. 8(b)] and therefore confirm our analytical prediction that the stability conditions (24) are typically violated first through  $q_2(t)$  when  $\beta$  increases and  $2N > M$ , rendering the second cluster unstable. A representative example is the point  $D$ , which lies in the stability regions of Figs. 8(a) and 8(c) and in the instability region of Fig. 8(b). This point corresponds to a one-headed chimera with the “head” being an incoherent state represented by the unstable second cluster and the “shoulders” determined by the first and third stable clusters (see Fig. 10).

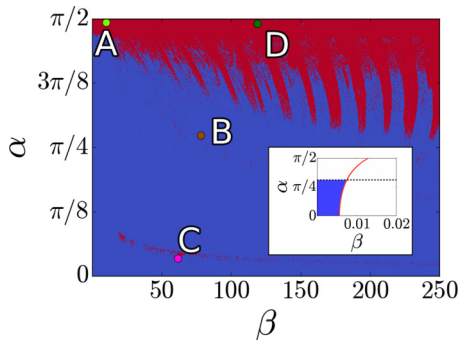


FIG. 9. Complete diagram for the stability of the three-cluster manifold  $C_{\Theta\Phi\Psi}$  from the combination of the three stability diagrams in Fig. 8. Blue indicates regions where all three clusters are stable, and red indicates regions where at least one cluster is unstable. The inset demonstrates the conservative analytical condition (24), with its left-hand side bound  $\alpha = \arccos \sqrt{2}\gamma$  and right-hand side bound  $\alpha = \arccos \frac{1-8\beta\gamma N}{4\beta M}$  plotted by the black dashed and red solid lines, respectively.

### B. Coexisting clusters and solitary-chimera states

The initial conditions for calculating the stability diagrams in Fig. 8 were chosen close to the three-cluster solution  $C_{\Theta\Phi\Psi}$  by perturbing the initial cluster state

$$\begin{aligned} \Theta(0) &= 0, \quad \Phi(0) = 0, \quad \Psi(0) = 2, \\ \dot{\Theta}(0) &= -1, \quad \dot{\Phi}(0) = 0, \quad \dot{\Psi}(0) = -2, \end{aligned} \quad (32)$$

with an offset  $\varepsilon_l$ ,  $l = 1, 2N + M$  of phases  $\Theta_i$  ( $i = 1, \dots, N$ ),  $\Phi_j$  ( $j = 1, \dots, M$ ), and  $\Psi_k$  ( $k = 1, \dots, N$ ). This offset is spread across the network, linearly increasing from the first oscillator in the first group with  $\varepsilon_1 = 0.000014$  to the last oscillator in the third group with  $\varepsilon_{2N+M} = \Delta = 0.001$ .

To study the nonlocal stability of synchronization within each of the three cluster groups, we numerically investigate the corresponding basins of attraction. This is performed by calculating the order parameter  $r$  for each cluster group,  $\Theta$ ,  $\Phi$ , and  $\Psi$ , as a function of the initial phase difference  $\Delta$  (see Fig. 11). The basins of attraction can be highly irregular and depend on the choice of the initial cluster state. More specifically, our simulations indicate that the rotating-rotating chaotic phase shift regime from point  $B$  in Fig. 8 is fragile

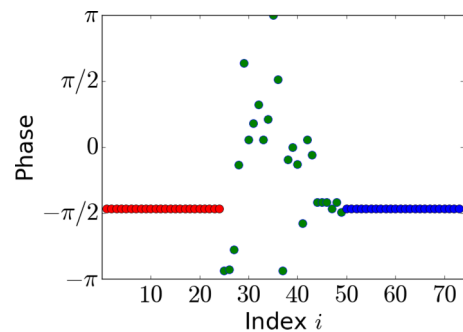


FIG. 10. Snapshot of a one-headed chimera corresponding to point  $D$  in Fig. 8. The oscillators from the second cluster form an incoherent state representing the “head” of the chimera. The phases of oscillators from the first and third clusters are synchronized and rotate around the cylinder in unity, with  $y = \Theta - \Psi = 0$ .

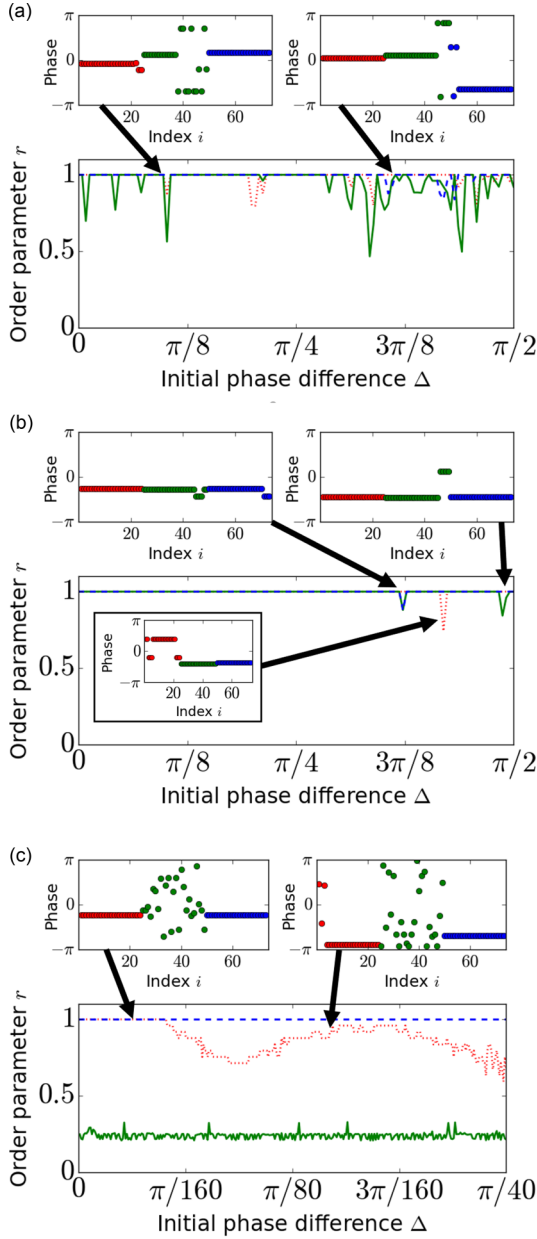


FIG. 11. Stability of synchronization within each of three cluster groups,  $\Theta$ ,  $\Phi$ ,  $\Psi$ , as a function of maximum initial phase difference  $\Delta$ . Order parameter  $r$  is calculated separately for phases  $\Theta_1 \cdots \Theta_N$  (red dotted line),  $\Phi_1 \cdots \Phi_M$  (green solid line), and  $\Psi_1 \cdots \Psi_N$  (blue dashed line). (a) The attraction basin of the three-cluster solution  $C_{\Theta\Phi\Psi}$  from point  $B$  in Fig. 8 is highly irregular. The left subplot presents a snapshot of a chimera with only oscillators within the third group (blue) remaining fully synchronized with  $r = 1$ . The right subplot represents a chimera with the first group (red) being the coherent state with  $r = 1$ . (b) Wide attraction basin of the three-cluster solution  $C_{\Theta\Phi\Psi}$  from point  $B$ . A significant increase of  $\Delta$  up to  $3\pi/8$  yields three different chimera states (three subplots). (c) Coexistence of two chimera states corresponding to point  $D$  from Fig. 8, at which the cluster solution  $C_{\Theta\Phi\Psi}$  is unstable. The one-headed chimera of Fig. 10 (left subplot) remains stable up to  $\pi/190$ . Note the emergence of solitary states in a region of  $\Delta$  between  $\pi/80$  and  $3\pi/160$ , where the red dotted curve approaches  $r = 1$ . The initial cluster state is chosen and perturbed as in (32). The plots are displayed after a transient time  $T = 10^4$ .

and disintegrates as the initial phase difference  $\Delta$  is initially increased, giving rise to solitary states and chimeras [Fig. 11(a)], when the initial cluster state (32) is chosen. Remarkably, this cluster pattern regains its stability with a further increase in  $\Delta$  and stays stable in a fairly large interval starting from about  $\Delta = \pi/8$ . The rotating-oscillating chaotic phase shift regime from point  $C$  in Fig. 8 is robust and remains stable up to the initial phase difference  $\Delta = 3\pi/8$ . A further increase of  $\Delta$  yields three different solitary states where only very few oscillators within one or two oscillator groups become incoherent [Fig. 11(b)]. Figure 11(c) demonstrates the coexistence of the one-headed chimera corresponding to point  $D$  in Fig. 8 with a hybrid solitary-chimera state (right subplot) where (i) the first group (red) with 3 out of 24 oscillators being out of synchrony represents a solitary state, (ii) the second group (green) corresponds to an incoherent state, and (iii) the third group represents a fully coherent state. It is important to emphasize that a different choice of the initial cluster state  $\Theta(0) = 0$ ,  $\Phi(0) = 0$ ,  $\Psi(0) = \pi$ ,  $\dot{\Theta}(0) = 0$ ,  $\dot{\Psi}(0) = 0$ ,  $\dot{\Phi}(0) = 0$  significantly enlarges the attraction basin of  $C_{\Theta\Phi\Psi}$  at points  $B$  and  $C$ . That is, the cluster pattern  $C_{\Theta\Phi\Psi}$  remains stable across the full range of initial phase difference  $\Delta$ , varying from 0 to  $\pi/2$ . In terms of Fig. 11, this would imply that the order parameter  $r$  for each of the three cluster groups would remain equal to 1 for  $\Delta \in [0, \pi/2]$ , yielding a trivial diagram with three (red, green, and blue) horizontal lines  $r = 1$  that is therefore not shown.

### C. Stability of the embedded two-cluster manifold

The diagrams in Figs. 8 and 9 provide plenty of insight into the stability of synchronization within the three cluster groups and therefore indicate when the three-cluster manifold  $C_{\Theta\Phi\Psi}$  is locally stable. However, the stability of  $C_{\Theta\Phi\Psi}$  does not necessarily imply the emergence of the corresponding three-cluster pattern with distinct phase shifts  $x$  and  $z$ . This is due to the fact that the cluster manifold  $C_{\Theta\Phi\Psi}$  contains the submanifold  $C_{\Theta\Phi\Theta}$  [see (4)] which represents the largest possible cluster partition of network (2) into two clusters where the first and third groups of synchronized oscillators form one cluster, making the phase shifts  $x$  and  $z$  equal.

In the following, we will analyze the conditions under which the two-cluster solution  $C_{\Theta\Phi\Theta}$  is stable and therefore determine which of the two cluster patterns defined by  $C_{\Theta\Phi\Psi}$  and  $C_{\Theta\Phi\Theta}$  can stably appear in the network.

Like for phase shifts  $x$  and  $z$ , we introduce the phase difference  $y = \Theta - \Psi$  between the phases of the synchronized oscillators in the first and third cluster groups. Note that  $y = z - x$ . As  $\Theta = \Psi$  on the cluster manifold  $C_{\Theta\Phi\Theta}$ , the stability of solution  $y = 0 : \{x = z\}$  implies the stability of  $C_{\Theta\Phi\Theta}$  within the larger cluster manifold  $C_{\Theta\Phi\Psi}$ .

The dynamics on the cluster manifold  $C_{\Theta\Phi\Theta}$  is governed by the equation

$$\beta\ddot{x} + \dot{x} = \Omega - \gamma[2N \sin(x - \alpha) + M \sin(x + \alpha)], \quad (33)$$

obtained from (6) by replacing  $z$  with  $x$ . Combining the sine terms, we obtain

$$\beta\ddot{x} + \dot{x} + R_1 \sin(x + \delta_2) = \Omega, \quad (34)$$

where  $R_1 = \gamma\sqrt{4N^2 + M^2 + 4MN \cos 2\alpha}$  and  $\delta_2 = \arctan\left(\frac{M-2N}{M+2N} \tan \alpha\right)$ ; the derivation of this equation is similar to that in [60]. Equation (34) is a 2D pendulum equation which cannot exhibit complex dynamics, so that the phase shift  $x = z$  can only be constant or can periodically rotate from  $-\pi$  to  $\pi$  as in the classical pendulum equation with a constant torque [70].

The stable constant phase shift

$$x_e = \arcsin \frac{\Omega}{R_1} - \delta_2 \quad (35)$$

is defined by a stable fixed point  $E_1(x_e)$  of 2D pendulum equation (34), which corresponds to the fixed point  $O_1(x_s = x_e + \delta_0)$  of 4D system (8). Equation (34) also has a saddle point  $E_2(x_{sd})$  corresponding to the phase shift

$$x_{sd} = \pi - \arcsin \frac{\Omega}{R_1} + \delta_2. \quad (36)$$

The rotating phase shift  $x_c(t)$  is determined by a stable limit cycle which is born as a result of a homoclinic bifurcation of saddle  $E_2$  (see [60] for more details on the analysis of the phase shift dynamics in this 2D case).

To analyze the stability of cluster manifold  $C_{\Theta\Phi\Theta}$  within  $C_{\Theta\Phi\Psi}$ , we derive the following equation for the difference  $y = z - x$ :

$$\ddot{y} + \dot{y} = \gamma M [\sin(x + \alpha) - \sin(z + \alpha)], \quad (37)$$

obtained by subtracting the  $x$  equation from the  $z$  equation in (6). Using a simple trigonometric identity, we obtain

$$\ddot{y} + \dot{y} = -2\gamma M \sin(y/2) \cos(y/2 + x + \alpha). \quad (38)$$

In the limit of infinitesimal  $y$  when  $\sin(y/2) \approx y/2$  and  $\cos(y/2 + x + \alpha) \approx \cos(x + \alpha)$ , we turn (38) into the equation

$$\ddot{y} + \dot{y} + \gamma M \cos(x + \alpha)y = 0, \quad (39)$$

which determines the local stability of the origin corresponding to phase shift  $y = 0$ . Note that (39) is a linear equation with a coefficient which is governed by phase shift  $x$  that may be constant or vary in time.

*Case I: Constant phase shift  $x_e$ .* In this simple case, Eq. (39) becomes a linear equation with a constant coefficient. As a result, it is stable at fixed point  $E_1(x_e)$  iff

$$\cos(x_e + \alpha) > 0, \quad (40)$$

yielding the condition  $\alpha < \pi/2 - x_e$ . Thus, we obtain the following necessary and sufficient condition for the local stability of cluster solution  $C_{\Theta\Phi\Theta}$  with a constant phase shift  $x_e$ :

$$\alpha < \alpha_{cr} = \pi/2 - \arcsin \frac{\Omega}{R_1} + \delta_2, \quad (41)$$

provided that  $\Omega = (M - N) \sin \alpha \leq R_1$ , ensuring the existence of fixed point  $E_1(x_e)$ .

Checking the stability condition (40) for the saddle point  $E_2(x_{sd})$  with  $x_{sd}$  defined in (36), we obtain the inequality  $\alpha < \pi/2 - x_{sd}$  which guarantees that saddle  $E_2(x_{sd})$  is locally stable in the transversal direction to  $C_{\Theta\Phi\Theta}$ . Substituting (36)

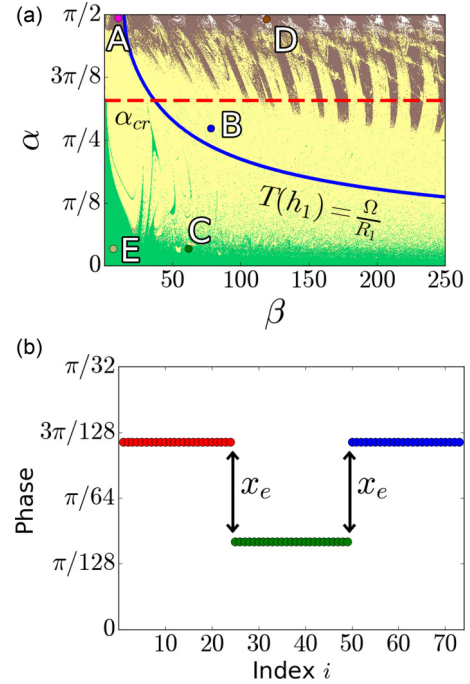


FIG. 12. (a) Stability diagram of the two-cluster solution  $C_{\Theta\Phi\Theta}$  with  $y = z - x = 0$ . Green indicates stability regions where  $C_{\Theta\Phi\Theta}$  with a constant phase shift  $x_c = z_c$  is stable ( $y = 0$  is stable). Yellow depicts regions where  $C_{\Theta\Phi\Theta}$  is unstable for the chosen initial conditions but the three-cluster solution  $C_{\Theta\Phi\Psi}$  with time-varying shifts  $x(t)$  and  $z(t)$  is stable. Brown indicates regions where both  $C_{\Theta\Phi\Theta}$  and  $C_{\Theta\Phi\Psi}$  are unstable. White depicts the regions where one-headed chimeras with stable  $y = \Theta - \Psi = 0$  emerge (the chimera of Fig. 10 is an example). Sample points A, B, C, and D are as in Figs. 8 and 9. Points B and C lie in the instability (yellow) regions of  $y = 0$ . The region under the horizontal dashed line  $\alpha = \alpha_{cr} = 1.0335$  corresponds to the stability condition (41). Sample point E lies in the stability region. The blue solid line indicates the Tricomi homoclinic curve  $\Omega/R_1 = T(h_1)$  in system (34). Initial conditions and other parameters are as in Figs. 8 and 9. (b). Snapshot of the two-cluster pattern with constant phase shift  $x_e$ , corresponding to point E.

into this inequality yields  $\alpha < x_e - \pi/2$ , which becomes the following transversal stability condition for saddle  $E_2(x_{sd})$ :

$$\alpha < \alpha^* = -\pi/2 + \arcsin \frac{\Omega}{R_1} - \delta_2 = -\alpha_{cr}. \quad (42)$$

Comparing (41) and (42), we conclude that two fixed points  $E_1(x_e)$  and  $E_2(x_{sd})$  cannot be stable simultaneously, so that the transversal stability of point  $E_1(x_e)$  guarantees the transversal instability of saddle  $E_2(x_{sd})$  on cluster manifold  $C_{\Theta\Phi\Theta}$ . This property provides an escape mechanism by which trajectories close to saddle  $E_2(x_{sd})$  can leave  $C_{\Theta\Phi\Theta}$ , while staying on the larger-dimensional manifold  $C_{\Theta\Phi\Psi}$  when the latter is stable. This leads to the *bistability* of two cluster patterns which is indeed observed in the network [see Fig. 12(a)]. Notice that the initial conditions used for generating the stability diagrams in Figs. 8 and 9 yield the instability of the two-cluster solution  $C_{\Theta\Phi\Theta}$  with a time-varying phase shift at points B and C [Fig. 12(a)]. However, the analytical condition (41) (red horizontal dashed line) guarantees that the two-cluster solution  $C_{\Theta\Phi\Theta}$  with a constant phase shift  $x_e = z_e$  is locally

stable at points  $B$  and  $C$ . This is in perfect agreement with the above stability argument and indicates the bistability of the coexisting three-cluster solution  $C_{\Theta\Phi\Psi}$  with the chaotic shifts (see Figs. 6 and 7) and the two-cluster pattern  $C_{\Theta\Phi\Theta}$  with the constant phase shift  $x_e = z_e$ . We have numerically verified that the attraction basin of this two-cluster solution is significantly smaller than that of the three-cluster solution with the chaotic phase shifts (not shown). This bistability is present in a large region of parameters (the yellow region under the red dashed line) and ceases to exist for smaller values of parameter  $\alpha$  (the green region). Sample point  $E$  corresponds to the two-cluster solution  $C_{\Theta\Phi\Theta}$  with a constant phase shift [Fig. 12(b)] which remains stable as guaranteed by the stability condition (41), whereas the three-cluster solution becomes unstable.

A comparison of the stability diagram in Fig. 12(a) with the existence diagram in Fig. 3 suggests that the three-cluster pattern defined by  $C_{\Theta\Phi\Psi}$  with constant phase shifts  $x(t) \neq z(t)$  does not stably appear in the network, at least for the chosen initial conditions. To verify this claim, one should notice that the existence region of  $C_{\Theta\Phi\Psi}$  with constant phase shifts  $x(t) \neq z(t)$  (the highly irregular white region in Fig. 3) coincides with the stability region for the two-cluster pattern  $C_{\Theta\Phi\Theta}$  with a constant shift  $x_e = z_e$  [the green region in Fig. 12(a)]. As a result, this three-cluster pattern becomes transient and eventually transforms into the two-cluster pattern with a constant shift.

*Case II: Rotating phase shift  $x_c(t)$ .* A stable limit cycle  $x_c(t)$  exists in the pendulum system (34) when  $\Omega/R_1 > T(h_1)$ , where  $T(h_1)$  is the Tricomi homoclinic curve (18) with  $h_1 = 1/\sqrt{\beta R_1}$ . Since  $x_c(t)$  periodically varies from  $-\pi$  to  $\pi$ , the factor  $\cos(x + \alpha)$  in (39) oscillates between positive and negative numbers. Therefore, the stability condition  $\cos[x_c(t) + \alpha] > 0$  may be satisfied only on average, thereby preventing a general analytical analysis and requiring the use of numerical simulations. However, we manage to approximately estimate the stability of  $\cos[x_c(t) + \alpha] > 0$  in a particular case where parameters  $\beta$  and  $\alpha$  are chosen to be slightly above the Tricomi homoclinic curve  $\Omega/R_1 = T(h_1)$  [the blue solid line in Fig. 12(a)]. Here, the stable limit cycle  $x_c(t)$  inherits the shape of the homoclinic orbit of  $E_2(x_{sd})$  from which it was born. Therefore, the limit cycle spends most of the time in the vicinity of saddle  $E_2(x_{sd})$  with the exception of a comparably short time of switching from  $x_{sd}$  to  $x_{sd} + 2\pi$ , so that  $x_c(t) \approx x_{sd}$ . Therefore, the condition for its transversal stability can be approximated as follows:

$$\cos[x_c(t) + \alpha] \approx \cos(x_{sd} + \alpha) > 0, \quad (43)$$

which coincides with condition (42) for the transversal stability of saddle  $E_2(x_{sd})$ . This implies that the stability condition (43) cannot be satisfied as long as the two-cluster solution  $C_{\Theta\Phi\Theta}$  with a constant phase shift  $x_e$  is stable [see (41) and (42)]. Hence, we can conclude that the two-cluster pattern  $C_{\Theta\Phi\Theta}$  with a rotating phase shift  $x_c(t) = z_c(t)$  is unstable in a parameter region slightly above the Tricomi homoclinic curve  $\Omega/R_1 = T(h_1)$  and below the stability line  $\alpha = \alpha_{cr}$  (red dashed line). Sample point  $B$  is located in this parameter region; our numerical simulations confirm that the two-cluster pattern  $C_{\Theta\Phi\Theta}$  with a time-varying shift  $x_c(t)$  is unstable at point  $B$ , thereby preserving the bistability of the three-cluster

pattern  $C_{\Theta\Phi\Psi}$  with a chaotic rotating-rotating phase shift and the two-cluster pattern  $C_{\Theta\Phi\Theta}$  with a constant phase shift.

## V. CONCLUSIONS AND DISCUSSION

The classical Kuramoto model of coupled first-order phase oscillators is known to exhibit various forms of spatiotemporal chaotic behavior, including phase chaos [43], mean-field chaotic dynamics in infinite [38] and finite-size networks [75,76], chaotic weak chimeras [64,77], and chaotic transients [78]. The emergence of chaos in the macroscopic dynamics of the Kuramoto model is traditionally attributed to oscillators' heterogeneity (see [38,79] and references therein). However, it was also shown that even symmetric systems of identical oscillators can induce chaotic dynamics in small-size Kuramoto networks of two populations [75,76].

In this paper, we have revealed and carefully analyzed a different form of chaotic behavior such as chaotic intercluster phase dynamics in a three-group network of identical second-order Kuramoto oscillators with inertia. The groups have different sizes and can split into clusters where the oscillators synchronize within a cluster while there is a pairwise phase shift between the dynamics of the clusters. Due to the presence of inertia, which increases the dimensionality of the oscillator dynamics, these phase shifts can exhibit different forms of chaotic behavior, including oscillatory, rotatory, and mixed-mode oscillations. We demonstrated that the phase shift dynamics is governed by a 4D system of two nonlinearly coupled driven pendulums. We have applied an auxiliary system approach to analyzing possible solutions of the 4D system and derived bounds on parameter partitions that support the coexistence of different chaotic intercluster dynamics. A representative example of these dynamics is a regime in which the phase shift between the first and second groups of oscillators chaotically oscillates within a small phase range, while the phase shift between the second and third groups chaotically rotates from  $-\pi$  to  $\pi$ . The bounds that separate the parameter regions of oscillatory and rotatory dynamics are explicit in the parameters of the network model. Therefore, they clearly highlight possible routes of transitions between the chaotic dynamics which can be induced by varying only one control parameter such as phase lag  $\alpha$  or inertia  $\beta$ . To identify a primary cause of chaotic dynamics in the 4D system, we have proved the existence of a Shilnikov homoclinic orbit to a saddle focus which leads to the emergence of spiral chaos [68].

Remarkably, the addition of only one oscillator to the three-group network with equal group sizes  $M = N$ , which yields asymmetry and the existence of the three-cluster pattern, is sufficient to induce large-amplitude chaotic oscillations of the phase shifts. Our extensive numerical analysis not reported in this paper also suggests that, in contrast to one's expectations, smaller differences in the group sizes are more effective in promoting phase shift chaos. Ultimately, the smallest network which can exhibit chaotic phase shifts consists of four second-order oscillators, with two oscillators forming the second group ( $M = 2$ ) and one oscillator in each of the first and third groups ( $N = 1$ ). The chosen network setup with no direct connections between the first and third groups could be viewed as an optimal configuration which minimizes the

complexity of the governing 4D system. Connecting the two groups could make the phase shift dynamics even richer, but it would introduce additional terms and make the 4D system less tractable analytically. Extending our analysis of intercluster phase dynamics to finer cluster partitions within each group, including solitary cluster states, is possible. However, the governing system will have a high dimension and might not necessarily be represented by a system of well separated coupled pendulums. Again, rigorous analysis of its possible chaotic states and transitions between them becomes more challenging. These problems are a subject of future study.

We have also analyzed the stability of the three-cluster pattern and its embedding, a two-cluster pattern, in which the first and third groups of oscillators become synchronized. Our analysis has explicitly demonstrated that the phase shift dynamics can be multistable, including the case where the three-cluster pattern with a chaotically oscillating phase shift stably coexists with the two-cluster pattern with a constant shift. Our stability conditions also have implications for the emergence of chimera states. Due to the simple network structure, these conditions are uncoupled and are applied to each group of oscillators separately. Thus, the simultaneous fulfillment of the stability condition for synchronization within one group and its failure for synchronization within the others can offer a key to predicting the emergence of a chimera state. These observations are in good agreement with our numerical results that confirmed the emergence of a plethora of coexisting chimera states in the network.

Our analysis can also be extended to networks with evolving [80], stochastically switching [81], or adaptive connections [82]. These networks exhibit highly nontrivial dynamics, including the emergence of macroscopic chaos [83,84], ghost attractors [85], and windows of opportunity [86,87] due to time-varying coupling. The role of time-varying connections in the emergence of stable or metastable clusters and ghost patterns in Kuramoto networks with inertia should be explored.

Although our analysis provides an unprecedented understanding of the emergence and coexistence of stable clusters with chaotic intercluster phase dynamics, we have only scratched the surface of the complex interplay between the existence of possible clusters, intrinsic oscillator dynamics, and nonlinear interactions of phases. The richness of the dynamics in our fairly simple and analytically tractable network model opens the door to further discovering new types of dynamical effects and cooperative structures in multipopulation networks of phase oscillators with inertia.

#### ACKNOWLEDGMENTS

This work was supported by the US National Science Foundation under Grant No. DMS-1909924 (to B.N.B. and I.V.B.), the RSF under Grant No. 19-12-00367 (qualitative analysis; to V.N.B.), and the Ministry of Science and Higher Education of the Russian Federation under Grant No. 0729-2020-0036 (to I.V.B. and V.N.B.). B.N.B. also acknowledges support through a Georgia State University Brains and Behavior Program Student Fellowship.

#### APPENDIX A: FIXED POINTS $O_3$ AND $O_4$

In this Appendix, we provide detailed calculations of coordinates  $x_{3,4}$  and  $z_{3,4}$  in (11) that correspond to fixed points  $O_3$  and  $O_4$  in 4D system (8), which governs the dynamics of intercluster phase shifts  $x$  and  $z$ .

To find the coordinates of  $O_3$  and  $O_4$  in 4D system (8), we need to analyze the following system:

$$\begin{aligned}\sin x + a \sin(z - \delta) &= \omega, \\ a \sin(x - \delta) + \sin z &= \omega.\end{aligned}\quad (\text{A1})$$

However, this analysis is not straightforward as one has to deal with a system of two nonlinear equations. A way to solve the system (A1) is to use its symmetry under the involution  $(x, z) \rightarrow (z, x)$ . This symmetry implies that  $O_3$  and  $O_4$  are symmetric relative to  $z = x$  and lie on the line

$$z = \kappa - x, \quad (\text{A2})$$

where  $\kappa$  is a constant to be determined. Thus, the coordinates of  $O_3$  and  $O_4$  can be written in the form

$$x_3 = z_4 = \kappa/2 + x_0, \quad x_4 = z_3 = \kappa/2 - x_0 \quad (\text{A3})$$

for some  $x_0$ . Substitution of (A2) into (A1) gives

$$\sin x + a \sin(-x + \kappa - \delta) = \omega. \quad (\text{A4})$$

Our goal is to find  $\kappa$  and  $x_0$  in order to identify coordinates  $x_3 = z_4$  and  $x_4 = z_3$ , the coordinates in (11). Using a trigonometric identity, we turn Eq. (A4) into

$$C_1 \cos x + [1 - a \cos(\kappa - \delta)] \sin x = \omega, \quad (\text{A5})$$

where  $C_1 = a \sin(\kappa - \delta)$ . Using another trigonometric identity, we solve Eq. (A5) for  $x$  to obtain

$$x_{3,4} = g \pm \arccos \frac{\omega}{C_2}, \quad (\text{A6})$$

$$C_2 = \sqrt{1 + a^2 - 2a \cos(\kappa - \delta)}, \quad (\text{A7})$$

$$g = \arctan \left( \frac{1 - a \cos(\kappa - \delta)}{C_1} \right). \quad (\text{A8})$$

From (A3) and (A6), we obtain  $g = \kappa/2$ , from which we calculate

$$\kappa/2 = \arctan \left( \frac{1 - a \cos \delta}{a \sin \delta} \right) \quad (\text{A9})$$

and then

$$\cos(\kappa - \delta) = \frac{2a - (a^2 + 1) \cos \delta}{a^2 + 1 - 2a \cos \delta}. \quad (\text{A10})$$

Thus, (A7) yields

$$C_2 = \frac{1 - a^2}{\sqrt{1 + a^2 - 2a \cos \delta}}, \quad (\text{A11})$$

so  $x_0$  in (A3) becomes

$$x_0 = \arccos \left( \frac{\omega \sqrt{1 + a^2 - 2a \cos \delta}}{1 - a^2} \right). \quad (\text{A12})$$

Substituting (A9) and (A12) into (A3), we finally obtain the explicit expressions (11) for  $x_3$ ,  $z_3$ ,  $x_4$ ,  $z_4$ .

## APPENDIX B: PROOF OF STATEMENT 1

In this Appendix, we derive the proof of Statement 1 and justify the parameter partition shown in Fig. 2. Adapting the auxiliary system method [71], we introduce two 2D auxiliary systems  $A_x^\pm$  obtained from the  $x$  equation of system (8) by replacing  $\sin(z - \delta)$  with  $\mp 1$ :

$$\begin{aligned} A_x^+ &: \ddot{x} + h\dot{x} + \sin x = \omega + a, \\ A_x^- &: \ddot{x} + h\dot{x} + \sin x = \omega - a. \end{aligned} \quad (\text{B1})$$

Similarly, we introduce the systems  $A_z^\pm$ :

$$\begin{aligned} A_z^+ &: \ddot{z} + h\dot{z} + \sin z = \omega + a, \\ A_z^- &: \ddot{z} + h\dot{z} + \sin z = \omega - a. \end{aligned} \quad (\text{B2})$$

Our goal is to demonstrate that the trajectories of auxiliary systems (B1) and (B2) bound trajectories of system (8) and govern their flow, thereby determining possible types of phase shift dynamics of  $x(t)$  and  $z(t)$  and predicting qualitative changes in the vector flow that are accompanied by homoclinic bifurcations. Our approach is based on the property that the vector flows of auxiliary systems (B1) and (B2) are transversal to any nontrivial trajectory of system (8) at each point on the cylinders  $(x, \dot{x})$ ,  $x \neq 0$ , and  $(z, \dot{z})$ ,  $z \neq 0$ . More specifically, the vertical component of vector fields  $(x, \dot{x})$  and  $(z, \dot{z})$  of systems  $A_x^\pm$  and  $A_z^\pm$  is larger than that of system (8), except for the points where  $\sin(z - \delta) = -1$  and  $\sin(x - \delta) = -1$  and systems (B1) and (B2) coincide with (8). As a result, the trajectories of system (8) cross the trajectories of systems  $A_x^+$  and  $A_x^-$  in the downward direction, and vice versa, the trajectories of system (8) cross the trajectories of systems  $A_x^-$  and  $A_x^+$  in the upward direction (see Fig. 13). Therefore, these properties allow for controlling the flow of system (8) with the help of separatrices and limit cycles of systems  $A_x^\pm$  and  $A_z^\pm$ . Recall that the 4D system (8) turns into two uncoupled 2D pendulum equations for  $x$  and  $z$  with  $a = 0$ . The dynamics of pendulum equation (17) in the parameter space  $(h, \omega)$  is controlled by the so-called Tricomi curve  $T(h)$ , Eq. (18) (see Fig. 2), which corresponds to a homoclinic bifurcation of a saddle fixed point for  $h < h^*$  and a saddle-node bifurcation for  $h > h^*$  [70] (see Fig. 2).

In terms of the bifurcation diagram  $(h, \omega)$  of Fig. 2, the Tricomi homoclinic curve  $T(h)$  (pink dashed line) and the saddle-node curve  $\omega = 1$  (green dash-dotted line) separate the bifurcation diagram into three regions with distinct dynamics of 2D pendulum equation (8) with  $a = 0$  for  $x$  or  $z$ . These dynamics are (i) a stable fixed point which coexists with a saddle fixed point [region under the Tricomi curve  $T(h)$ ], (ii) the coexistence of the stable fixed point and a limit cycle (region bounded by the Tricomi and saddle-node curves), and (iii) a globally stable limit cycle.

We adapt these baseline boundaries for auxiliary systems (B1) and (B2) with  $a \neq 0$  to derive sufficient conditions on permissible dynamics of 4D system (8), which in turn determines the existence of phase shift dynamics in the three-group network (2). The dynamics of auxiliary systems  $A_x^+$  and  $A_x^-$  ( $A_z^+$  and  $A_z^-$ ) are symmetric. Therefore, it is sufficient to characterize possible trajectories of systems  $A_x^+$  and  $A_x^-$  in the  $(x, \dot{x})$  projection which also yields the symmetrical trajectories in the  $(z, \dot{z})$  projection. A combination of two (identical

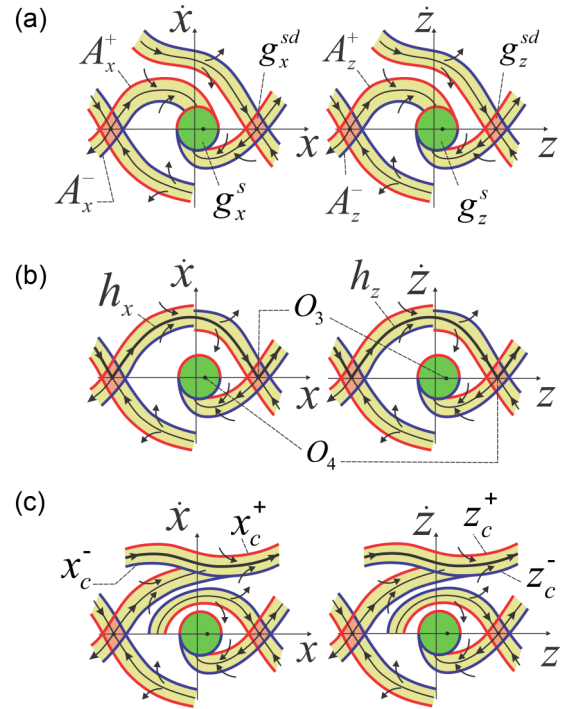


FIG. 13. Schematic diagrams for  $(x, \dot{x})$  and  $(z, \dot{z})$  projections of vector flow (8), bounded by the trajectories of 2D auxiliary systems  $A_x^+$  and  $A_x^-$  ( $A_z^+$  and  $A_z^-$ ) depicted in red (blue). (a) Typical arrangement of vector flow (8) corresponding to region I (see Fig. 2). The unstable manifolds of the auxiliary systems' saddles form trapping regions ("rivers") that attract the trajectories of system (8) and guide them into trapping disks  $g_x^s$  and  $g_z^s$  (green). (b) Arrangement of vector flow (8) from region II which allows the formation of the homoclinic orbit  $h_x$  ( $h_z$ ) of saddle focus  $O_3$  ( $O_4$ ). Note that the saddle focus  $O_3$  lies inside saddle cell  $g_x^{sd}$  (pink diamond-shaped region) in the  $(x, \dot{x})$  projection and inside stable region  $g_z^s$  (green disk) in the  $(z, \dot{z})$  projection, representing its focus part. Saddle-focus point  $O_4$  is symmetric to  $O_3$ , with its  $x$  ( $z$ ) coordinate inside  $g_x^s$  ( $g_z^s$ ). (c) Region III. The auxiliary systems are bistable, each having a stable fixed point and a stable limit cycle. These limit cycles  $x_c^+$  and  $x_c^-$  ( $z_c^+$  and  $z_c^-$ ) form a trapping river (the upper horizontal strip) which contains rotatory trajectories of (8). Trapping disks  $g_x^s$  and  $g_z^s$  (green) contain oscillatory trajectories of (8).

or different) dynamics in the  $(x, \dot{x})$  and  $(z, \dot{z})$  projections will represent the behavior of 4D system (8).

Notice that the presence of the  $+a$  ( $-a$ ) term in auxiliary system  $A_x^+$  ( $A_x^-$ ) shifts the bifurcation diagrams and yields the new Tricomi homoclinic curve  $\omega = T(h) - a$  ( $\omega = T(h) + a$ ) and the saddle-node curve  $\omega = 1 - a$  ( $\omega = 1 + a$ ) in system (B1). These curves formally partition the bifurcation diagram of Fig. 2 into five regions which correspond to the following dynamics.

*Region I:*  $\omega < T(h) - a$ . In this region both auxiliary systems  $A_x^+$  and  $A_x^-$  may have only trivial dynamics in the form of the stable fixed point coexisting with the saddle fixed point. Figure 13 shows the arrangement of typical trajectories of auxiliary systems  $A_x^+$  ( $A_z^+$ ) (red lines) and  $A_x^-$  ( $A_z^-$ ) (blue lines). The auxiliary system  $A_x^+$  has the stable fixed point  $E_x^+[x = \arcsin(\omega + a)]$  and the saddle  $S_x^+[x = \pi - \arcsin(\omega + a)]$  (not shown in Fig. 13). Similarly, the auxiliary system  $A_x^-$  has the stable fixed point  $E_x^-[x = \arcsin(\omega - a)]$  and the saddle

$S_x^- [x = \pi - \arcsin(\omega - a)]$ . As a result, the trajectories of the two auxiliary systems which approach the corresponding stable fixed points  $E_x^-$  and  $E_x^+$  form a “river” which traps trajectories of system (8) in the  $(x, \dot{x})$  projection of the 4D phase space. Therefore, these trajectories of system (8) eventually reach the stable trapping region  $g_x^s$  bounded in  $x$  by  $E_x^-$  and  $E_x^+$  [the green disk in Fig. 13(a), left] and stay inside it. The dynamics of system (8) in the  $(z, \dot{z})$  projection is identical, so that there also exists a stable trapping region  $g_z^s$  [the green disk in Fig. 13(a), right]. These two disks form a topological ball  $g_x^s \times g_z^s$  in the 4D phase space of system (8) which contains the fixed point  $O_1$  (not shown). The dynamics inside the ball may be periodic or even chaotic; however, the trajectories confined inside the ball may not rotate around the cylinders  $(x, \dot{x})$  and  $(z, \dot{z})$ , so that only oscillatory motions with small amplitudes in  $x$  and  $z$  are allowed. Similarly, the stable manifolds of saddles  $S_x^+$  and  $S_x^-$  form a river which contains the saddle  $O_2$  of (8) (not shown) and the  $(x, \dot{x})$  projection of its stable manifold. However, due to the flow arrangement, other trajectories of (8) leave this river and the saddle “cell”  $g_x^{sd}$  formed by the stable and unstable manifolds of saddles  $S_x^+$  and  $S_x^-$  [the pink diamond-shaped region in Fig. 13(a), left] and approach the stable trapping zone. In the full 4D phase space of (8), the fixed point  $O_2$  lies in a region represented by a topological product of saddle cells  $g_x^{sd}$  and  $g_z^{sd}$ . At the same time, the fixed point  $O_3$  ( $O_4$ ) of (8) lies in the region  $g_x^{sd} \times g_z^s$  ( $g_x^s \times g_z^{sd}$ ).

*Region II:*  $H_1 : \{\omega < 1 - a\} \cap H_2 : \{\omega < T(h) + a\} \cap H_3 : \{\omega > T(h) - a\}$ . The lower border of region II (the gray region in Fig. 2) is determined by the part of the Tricomi curve  $\omega = T(h) - a$  which corresponds to a homoclinic bifurcation of saddle  $E_x^-$  ( $E_z^-$ ) in auxiliary system  $A_x^-$  ( $A_z^-$ ). In terms of Fig. 13(a) (left panel), this bifurcation occurs when the red curve emanating from the left saddle cell  $g_x^{sd}$  (the pink diamond-shaped region) would no longer go towards the green disk but rather merge with the red curve going into the right saddle cell to form a homoclinic orbit which connects the left and right saddle cells  $g_x^{sd}$  (not shown). This homoclinic connection reroutes the vector flows so that the trajectories of system (8) can travel from the left to the right saddle cell. Entering the region II, via, for example, increasing  $\omega$  leads to the rearrangement of the rivers, as shown in Fig. 13(b) where the unstable manifold of saddle focus (or saddle)  $O_3$  returns to  $O_3$  and forms the homoclinic orbit  $h_x$ . Notice that due to the cyclic structure of the equations, the left and right saddle cells represent the same cell and contain the same fixed point  $O_3$ , so that the black curve connecting the fixed points in the two saddle cells is a homoclinic (not heteroclinic) orbit. The mutual arrangement of the rivers in the region  $\dot{x} > 0$  allows the trajectories to either rotate around the cylinder as in the case of the homoclinic loop or reach the green disk to exhibit oscillatory dynamics. As the dynamics of systems  $A_z^+$  and  $A_z^-$  are symmetric to those of systems  $A_x^+$  and  $A_x^-$ , the overall dynamics of 4D system (8) is a combination of the trajectories depicted in the left and right diagrams of Fig. 13(b). Therefore, all combinations of rotating, oscillating, and mixed-mode phases shifts are possible.

While this qualitative analysis does not allow for determining the exact values of parameters at which the homoclinic loop  $h_x$  is formed, it proves that system (8) has to undergo this homoclinic bifurcation in region II where the rivers form

a passage from one saddle cell to the other. This passage does not exist for the parameters from region I [see Fig. 13(a)] and ceases to exist when the system reaches the border of region III at which auxiliary systems  $A_x^+$  and  $A_z^+$  undergo a homoclinic bifurcation at  $\omega = T(h) + a$  (see Fig. 2). In terms of Fig. 13(b), this happens when the unstable and stable manifolds of saddle  $S_x^+$  in system  $A_x^+$  (the blue curves) merge together at the  $x = 0$  coordinate axis for  $\dot{x} > 0$  (not shown). Therefore, the rivers formed by the stable and unstable manifolds of the saddle in auxiliary systems  $A_x^+$  and  $A_x^-$  ( $A_z^+$  and  $A_z^-$ ) exchange their mutual arrangement when changing the parameters brings the system from region I to region III [see Figs. 13(a) and Fig. 13(c)]. Hence, there always exist bifurcation points in Region II at which the stable and unstable manifolds of  $O_3$  ( $O_4$ ), confined inside the rivers, form the homoclinic loop  $h_x$  ( $h_z$ ). Each of these bifurcation points lies on any path from region I to region III in parameter space  $(h, \omega)$ , which lies entirely inside region II. Since the passage from one saddle cell to the other exists only in region II, other multiloop homoclinic bifurcations of  $O_3$  and  $O_4$  may also be possible only in region II.

*Region III:*  $T(h) + a < \omega < 1 - a$ . Entering this region (the blue region in Fig. 2) from region II disconnects the rivers centered around the stable and unstable manifolds, as shown in Fig. 13(c). In region III, each system  $A_x^-$  and  $A_x^+$  is bistable and has a stable fixed point (inside the green disk) and a limit cycle of rotatory type, born as a result of the homoclinic bifurcations at  $\omega = T(h) - a$  and  $\omega = T(h) + a$ , respectively. Therefore, the trajectories of 4D system (8) eventually reach and remain trapped either inside the green disk or inside the river formed by two stable limit cycles  $x_c^-$  and  $x_c^+$  [the horizontal river in the upper part of Fig. 13(c), left]. As a result, this arrangement guarantees (i) the bistability of oscillatory and rotatory trajectories which may be periodic or chaotic and (ii) the absence of mixed-mode oscillations since the trajectories cannot switch between the two trapping regions. Again, combining the dynamics of the left and right diagrams of Fig. 13(c) guarantees the existence of rotating-rotating, rotating-oscillating, and oscillating-oscillating phase shift regimes in the network.

*Region IV:*  $1 - a < \omega < 1 + a$ . System  $A_x^+$  has only a stable limit as the stable and saddle fixed points  $E_x^+$  and  $S_x^+$  have disappeared via a saddle-node bifurcation at  $\omega = 1 - a$ . At the same time, system  $A_x^-$  has the same structure as in region III. In terms of Fig. 13(c), this amounts to the disappearance of all red curves (not shown), except for the upper border of the horizontal river representing the stable limit cycle  $x_c^+$ . As the trapping disk has partly disintegrated, the trajectories of the 4D system (8) may escape it and reach the trapping river with rotatory trajectories. Hence, all possible dynamics of phase shifts are possible, with the prevalence of rotatory trajectories.

*Region V:*  $\omega > 1 + a$ . Similar to system  $A_x^+$  at the border between region III and region IV, system  $A_x^-$  undergoes a saddle-node bifurcation at  $\omega = 1 + a$ . Thus, in region V both systems  $A_x^-$  and  $A_x^+$  have only globally stable limit cycles  $x_c^-$  and  $x_c^+$ , which form a unique trapping region (river) for all the system’s trajectories, yielding the existence of only rotatory trajectories in the system (8). ■

- [1] S. H. Strogatz, *Nature (London)* **410**, 268 (2001).
- [2] A. Pikovsky, M. Rosenblum, and J. Kurths, *Synchronization: A Universal Concept in Nonlinear Sciences*, Cambridge Non-linear Science Series, Vol. 12 (Cambridge University Press, Cambridge, 2003).
- [3] S. Boccaletti, V. Latora, Y. Moreno, M. Chavez, and D.-U. Hwang, *Phys. Rep.* **424**, 175 (2006).
- [4] P. S. Churchland and T. J. Sejnowski, *The Computational Brain* (MIT Press, Cambridge, MA, 2016).
- [5] K. Mizuseki and G. Buzsaki, *Philos. Trans. R. Soc. B* **369**, 20120530 (2014).
- [6] J. A. Wolf and P. F. Koch, *Front. Syst. Neurosci.* **10**, 43 (2016).
- [7] K. Schindler, C. E. Elger, and K. Lehnertz, *Clin. Neurophysiol.* **118**, 1955 (2007).
- [8] C. Hammond, H. Bergman, and P. Brown, *Trends Neurosci.* **30**, 357 (2007).
- [9] S. Camazine, J.-L. Deneubourg, N. R. Franks, J. Sneyd, E. Bonabeau, and G. Theraulaz, *Self-Organization in Biological Systems*, Princeton Studies in Complexity Vol. 7 (Princeton University Press, Princeton, NJ, 2003).
- [10] S. H. Strogatz, D. M. Abrams, A. McRobie, B. Eckhardt, and E. Ott, *Nature (London)* **438**, 43 (2005).
- [11] B. Eckhardt, E. Ott, S. H. Strogatz, D. M. Abrams, and A. McRobie, *Phys. Rev. E* **75**, 021110 (2007).
- [12] I. V. Belykh, R. Jeter, and V. N. Belykh, *Chaos* **26**, 116314 (2016).
- [13] I. Belykh, R. Jeter, and V. Belykh, *Sci. Adv.* **3**, e1701512 (2017).
- [14] R. Roy and K. S. Thornburg, Jr., *Phys. Rev. Lett.* **72**, 2009 (1994).
- [15] M. Prevedelli, T. Freegarde, and T. Hänsch, *Appl. Phys. B* **60**, s241 (1995).
- [16] J. Ding, I. Belykh, A. Marandi, and M.-A. Miri, *Phys. Rev. Appl.* **12**, 054039 (2019).
- [17] A. E. Motter, S. A. Myers, M. Anghel, and T. Nishikawa, *Nat. Phys.* **9**, 191 (2013).
- [18] L. M. Pecora and T. L. Carroll, *Phys. Rev. Lett.* **80**, 2109 (1998).
- [19] S. Boccaletti, J. Kurths, G. Osipov, D. Valladares, and C. Zhou, *Phys. Rep.* **366**, 1 (2002).
- [20] V. N. Belykh, I. V. Belykh, and M. Hasler, *Phys. D (Amsterdam, Neth.)* **195**, 159 (2004).
- [21] I. Belykh, E. de Lange, and M. Hasler, *Phys. Rev. Lett.* **94**, 188101 (2005).
- [22] V. N. Belykh, I. V. Belykh, and M. Hasler, *Phys. Rev. E* **62**, 6332 (2000).
- [23] V. N. Belykh, I. V. Belykh, and E. Mosekilde, *Phys. Rev. E* **63**, 036216 (2001).
- [24] A. Pogromsky and H. Nijmeijer, *IEEE Trans. Circuits Syst. I* **48**, 152 (2001).
- [25] A. Pogromsky, G. Santoboni, and H. Nijmeijer, *Phys. D (Amsterdam, Neth.)* **172**, 65 (2002).
- [26] I. Belykh, V. Belykh, K. Nevidin, and M. Hasler, *Chaos* **13**, 165 (2003).
- [27] M. Golubitsky, I. Stewart, and A. Török, *SIAM J. Appl. Dyn. Syst.* **4**, 78 (2005).
- [28] M. Golubitsky and I. Stewart, *Bull. Am. Math. Soc.* **43**, 305 (2006).
- [29] Y. Wang and M. Golubitsky, *Nonlinearity* **18**, 631 (2004).
- [30] L. M. Pecora, F. Sorrentino, A. M. Hagerstrom, T. E. Murphy, and R. Roy, *Nat. Commun.* **5**, 4079 (2014).
- [31] I. Belykh and M. Hasler, *Chaos* **21**, 016106 (2011).
- [32] H. Kamei and P. J. Cock, *SIAM J. Appl. Dyn. Syst.* **12**, 352 (2013).
- [33] F. Sorrentino, L. M. Pecora, A. M. Hagerstrom, T. E. Murphy, and R. Roy, *Sci. Adv.* **2**, e1501737 (2016).
- [34] Y. Kuramoto, *International Symposium on Mathematical Problems in Theoretical Physics* (Springer, Berlin, 1975), pp. 420–422.
- [35] S. H. Strogatz, *Phys. D (Amsterdam, Neth.)* **143**, 1 (2000).
- [36] J. A. Acebrón, L. L. Bonilla, C. J. P. Vicente, F. Ritort, and R. Spigler, *Rev. Mod. Phys.* **77**, 137 (2005).
- [37] E. Barreto, B. Hunt, E. Ott, and P. So, *Phys. Rev. E* **77**, 036107 (2008).
- [38] E. Ott and T. M. Antonsen, *Chaos* **18**, 037113 (2008).
- [39] E. A. Martens, E. Barreto, S. H. Strogatz, E. Ott, P. So, and T. M. Antonsen, *Phys. Rev. E* **79**, 026204 (2009).
- [40] H. Hong, H. Chaté, H. Park, and L.-H. Tang, *Phys. Rev. Lett.* **99**, 184101 (2007).
- [41] A. Pikovsky and M. Rosenblum, *Phys. Rev. Lett.* **101**, 264103 (2008).
- [42] Y. Maistrenko, O. Popovych, O. Burylko, and P. A. Tass, *Phys. Rev. Lett.* **93**, 084102 (2004).
- [43] O. V. Popovych, Y. L. Maistrenko, and P. A. Tass, *Phys. Rev. E* **71**, 065201(R) (2005).
- [44] Y. Kuramoto and D. Battogtokh, *arXiv:cond-mat/0210694* (2002).
- [45] D. M. Abrams and S. H. Strogatz, *Phys. Rev. Lett.* **93**, 174102 (2004).
- [46] D. M. Abrams, R. Mirollo, S. H. Strogatz, and D. A. Wiley, *Phys. Rev. Lett.* **101**, 084103 (2008).
- [47] M. J. Panaggio and D. M. Abrams, *Nonlinearity* **28**, R67 (2015).
- [48] O. E. Omelchenko, *Nonlinearity* **26**, 2469 (2013).
- [49] M. Wolfrum, O. E. Omelchenko, S. Yanchuk, and Y. L. Maistrenko, *Chaos* **21**, 013112 (2011).
- [50] C. R. Laing, *Phys. Rev. E* **100**, 042211 (2019).
- [51] P. Ashwin and O. Burylko, *Chaos* **25**, 013106 (2015).
- [52] M. J. Panaggio, D. M. Abrams, P. Ashwin, and C. R. Laing, *Phys. Rev. E* **93**, 012218 (2016).
- [53] B. Ermentrout, *J. Math. Biol.* **29**, 571 (1991).
- [54] L. Tumash, S. Olmi, and E. Schöll, *Chaos* **29**, 123105 (2019).
- [55] H.-A. Tanaka, A. J. Lichtenberg, and S. Oishi, *Phys. Rev. Lett.* **78**, 2104 (1997).
- [56] H.-A. Tanaka, A. J. Lichtenberg, and S. Oishi, *Phys. D (Amsterdam, Neth.)* **100**, 279 (1997).
- [57] P. Ji, T. K. Peron, F. A. Rodrigues, and J. Kurths, *Sci. Rep.* **4**, 4783 (2015).
- [58] V. Munyaev, L. Smirnov, V. Kostin, G. Osipov, and A. Pikovsky, *New J. Phys.* **22**, 023036 (2020).
- [59] S. Olmi, A. Navas, S. Boccaletti, and A. Torcini, *Phys. Rev. E* **90**, 042905 (2014).
- [60] I. V. Belykh, B. N. Brister, and V. N. Belykh, *Chaos* **26**, 094822 (2016).
- [61] S. Olmi, *Chaos* **25**, 123125 (2015).
- [62] M. Komarov, S. Gupta, and A. Pikovsky, *Europhys. Lett.* **106**, 40003 (2014).
- [63] P. Jaros, S. Brezetsky, R. Levchenko, D. Dudkowski, T. Kapitaniak, and Y. Maistrenko, *Chaos* **28**, 011103 (2018).
- [64] Y. Maistrenko, S. Brezetsky, P. Jaros, R. Levchenko, and T. Kapitaniak, *Phys. Rev. E* **95**, 010203(R) (2017).

- [65] G. Yan, P. E. Vértes, E. K. Towilson, Y. L. Chew, D. S. Walker, W. R. Schafer, and A.-L. Barabási, *Nature (London)* **550**, 519 (2017).
- [66] J. Hizanidis, N. E. Kouvaris, G. Zamora-López, A. Díaz-Guilera, and C. G. Antonopoulos, *Sci. Rep.* **6**, 19845 (2016).
- [67] P. DeLellis, G. Polverino, G. Ustuner, N. Abaid, S. Macrì, E. M. Bollt, and M. Porfiri, *Sci. Rep.* **4**, 3723 (2014).
- [68] L. P. Shilnikov, *Dokl Akad. Nauk SSSR* **160**, 558 (1965).
- [69] V. N. Belykh, N. F. Pedersen, and O. H. Soerensen, *Phys. Rev. B* **16**, 4860 (1977).
- [70] A. A. Andronov, A. A. Vitt, and S. E. Khaikin, *Theory of Oscillators*, *Adiwes International Series in Physics* Vol. 4 (Elsevier, 2013).
- [71] V. N. Belykh and E. V. Pankratova, *Int. J. Bifurcation Chaos* **24**, 1440007 (2014).
- [72] F. Tricomi, *Ann. Sc. Normale Super. Pisa Classe Sci.* **2**, 1 (1933).
- [73] L. P. Shilnikov, A. L. Shilnikov, D. V. Turaev, and L. Chua, *Qualitative Theory in Nonlinear Dynamics, Part II* (World Scientific, Singapore, 2001).
- [74] B. P. Demidovich, *Lectures on Stability Theory* (Nauka, Moscow, 1967).
- [75] C. Bick, M. Timme, D. Paulikat, D. Rathlev, and P. Ashwin, *Phys. Rev. Lett.* **107**, 244101 (2011).
- [76] C. Bick, M. J. Panaggio, and E. A. Martens, *Chaos* **28**, 071102 (2018).
- [77] C. Bick and P. Ashwin, *Nonlinearity* **29**, 1468 (2016).
- [78] M. Wolfrum and O. E. Omel'chenko, *Phys. Rev. E* **84**, 015201 (2011).
- [79] P. S. Skardal, J. G. Restrepo, and E. Ott, *Phys. Rev. E* **91**, 060902(R) (2015).
- [80] I. Belykh, M. Di Bernardo, J. Kurths, and M. Porfiri, *Phys. D (Amsterdam, Neth.)* **267**, 1 (2014).
- [81] M. Hasler, V. Belykh, and I. Belykh, *SIAM J. Appl. Dyn. Syst.* **12**, 1031 (2013).
- [82] R. Berner, E. Scholl, and S. Yanchuk, *SIAM J. Appl. Dyn. Syst.* **18**, 2227 (2019).
- [83] P. So and E. Barreto, *Chaos* **21**, 033127 (2011).
- [84] P. S. Skardal, D. Taylor, and J. G. Restrepo, *Phys. D (Amsterdam, Neth.)* **267**, 27 (2014).
- [85] I. Belykh, V. Belykh, R. Jeter, and M. Hasler, *Eur. Phys. J. Spec. Top.* **222**, 2497 (2013).
- [86] R. Jeter and I. Belykh, *IEEE Trans. Circuit Syst. I: Regular Pap.* **62**, 1260 (2015).
- [87] O. Golovneva, R. Jeter, I. Belykh, and M. Porfiri, *Phys. D (Amsterdam, Neth.)* **340**, 1 (2017).